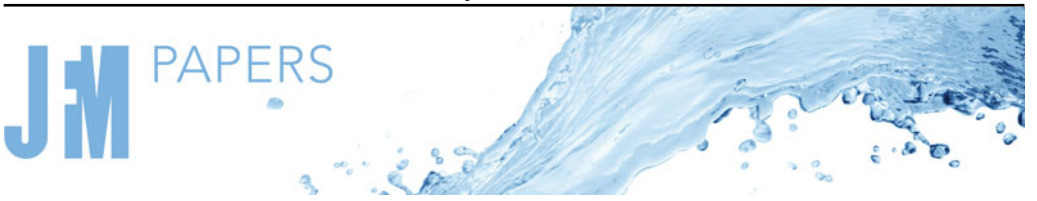
J. Fluid Mech. (2026), *vol.* 1037, A39, doi:10.1017/jfm.2026.11712



Dynamic interactions between a self-propelled flexible plate and multiple wall-mounted compliant blades

Xian-Guang Luo[1], **An-Kang Gao**[1], **Nan-Sheng Liu**[1] **and Xi-Yun Lu**[1]

[1]State Key Laboratory of High Temperature Gas Dynamics, School of Engineering Science, University of Science and Technology of China, Hefei 230027, PR China

Corresponding authors: An-Kang Gao; ankanggao@ustc.edu.cn; Xi-Yun Lu, xlu@ustc.edu.cn

(Received 1 January 2026 UTC; revised 20 May 2026 UTC; accepted 20 May 2026 UTC)

A numerical study is conducted on a self-propelled flexible plate moving above an array of wall-mounted compliant blades at Reynolds numbers of order 100, designed to mimic flatfish-like locomotion near the vegetation-covered seabed. Compared with a flat rigid wall located at the same vertical distance from the plate, the blade-covered wall enhances the propulsive performance of the plate, yielding a higher propulsive velocity and lower energy consumption per transport distance. This enhancement intensifies as the blade spacing and vertical distance between the plate and the bottom wall decrease, but diminishes when the flapping frequency approaches the natural frequency of the blades due to resonance. By accounting for the asymmetric motion of the plate during the upper and lower half-periods, a universal scaling law $Re_c \sim (Re_{f,\delta})^{3/2}$ is identified between the propulsive Reynolds number Re_c and the corrected flapping Reynolds number $Re_{f,\delta}$. Under the excitation of the flapping plate, two distinct vibration patterns are identified for the blade array. The first is the flapping-driven mode, which propagates synchronously with the plate's motion. The second exhibits forward-propagating travelling waves, which are generated by the cooperative underdamped vibrations of downstream blades, and have a phase velocity much faster than the propulsive velocity of the plate. This study may shed light on the design of bio-inspired underwater vehicles and flow sensing techniques.

Key words: swimming/flying, propulsion, flow-structure interactions

1. Introduction

Demersal fishes that live and forage near the seabed are ubiquitous in coastal and shallow-water environments (Moyle & Cech 2004; Gibson, Stoner & Ryer 2014;

© The Author(s), 2026. Published by Cambridge University Press. This is an Open Access article, distributed under the terms of the Creative Commons Attribution licence (https://creativecommons.org/licenses/by/4.0/), which permits unrestricted re-use, distribution and reproduction, provided the original article is properly cited.

https://doi.org/10.1017/jfm.2026.11712 Published online by Cambridge University Press

Fox *et al.* 2018). Adapted to such near-bottom habitats, numerous demersal species have evolved specialised locomotion strategies. For instance, the winter flounder (*Pleuronectes americanus*) remains extremely close to the seabed during locomotion, rarely ascending more than one and a half body lengths above the bottom, and frequently swimming with its posterior body nearly in contact with the substrate (He 2003). For demersal fishes, locomotion performance is determined not only by body kinematics but also by the benthic boundary and attached flexible structures, such as seagrass and macroalgae (Stoner & Titgen 2003; O'Leary *et al.* 2021). Understanding how demersal fishes interact with the seabed therefore provides fundamental insights into physical mechanics governing benthic swimming, and inspires the design of underwater robots operating in near-boundary environments (Liu *et al.* 2024).

The influence of the seabed (bottom wall) on fish locomotion is termed the ground effect, which modulates both the body kinematics and propulsive performance of swimmers. For instance, the tail-beat amplitude and maximum swimming velocity of steelhead trout (*Oncorhynchus mykiss*) decrease when swimming near the seabed, while their tail-beat frequency remains unchanged (Webb 1993). For the plaice (*Pleuronectes platessa*), a typical benthic fish, its tail-beat frequency increases with swimming velocity when moving near the seabed, but becomes independent of the velocity when swimming farther from the bottom (Webb 2002). Similarly, Nowroozi *et al.* (2009) observed that northern spearnose poacher (*Agonopsis vulsa*) use the ground effect to enhance lift when swimming within one centimetre of the seabed, thereby counteracting negative buoyancy. In a separate study, Yang *et al.* (2024) reported that brown trout (*Salmo trutta*) exhibit increased swimming velocity but decreased propulsive efficiency when their distance from the seabed is less than half a body length.

Despite the inherently three-dimensional (3-D) nature of fish swimming, it is widely recognised that the leading-order propulsive mechanisms are predominantly governed by the unsteady lateral motion of the tail and the associated vortex dynamics developing in the plane normal to the spanwise direction of the caudal fin (Smits 2019). Within this context, two-dimensional (2-D) models have been widely adopted as a minimal yet physically representative framework for investigating fish-like propulsive dynamics (Alben 2008; Alben *et al.* 2012; Zhu, He & Zhang 2014).

To explore the ground effect on flatfish-like propulsion, where the caudal fin primarily undergoes vertical oscillations above the seabed, aerofoils and flexible plates flapping near a rigid flat wall have been extensively studied. Employing both experimental and numerical methods, Quinn *et al.* (2014) investigated the hydrodynamic effects of a flat bottom wall on a rigid pitching aerofoil submerged in a free-stream flow. They observed that the average thrust of the aerofoil increases monotonically as the distance from the wall decreases, and further noted that concentrated vortices in the wake form upward-deflected vortex pairs rather than a reverse Bénard–von Kármán vortex street, thereby forming a mean momentum jet angled away from the wall. Additionally, an equilibrium height at which the average lift of the aerofoil attains zero has also been identified (Zhong *et al.* 2021; Han *et al.* 2024). Numerical studies on self-propelled flexible plates near a flat wall in a quiescent flow have been conducted by Dai, He & Zhang (2016), Tang *et al.* (2016), Park, Kim & Sung (2017) and Zhang, Huang & Lu (2017). These investigations revealed that in most cases, a rigid plate achieves a higher propulsive velocity near the bottom wall at the expense of increased energy consumption. However, a flexible plate with optimal stiffness exhibits enhancements in both propulsive velocity and energy efficiency. Jeong, Lee & Park (2021) further explored the collective motion of two tandem self-propelled flexible plates in the presence of zero, one or two side walls. They observed that the following plate exhibits a hybrid vortex interception–slalom locomotion pattern when side

https://doi.org/10.1017/jfm.2026.11712 Published online by Cambridge University Press

walls are present, which differs from the pure vortex interception mode observed without side walls. Furthermore, the overall efficiency of the plate pair is optimised under moderate wall proximity and bending rigidity.

It should be noted that the natural seabed is composed of sand, mud and aquatic vegetation (Van Katwijk *et al.* 2010), which exhibit pronounced fluid-induced deformations. In vegetative flows, coherent waving motions between adjacent plants emerge under certain conditions, a phenomenon known as monami (Ackerman & Okubo 1993). Both experimental observations (Ghisalberti & Nepf 2002; Fu *et al.* 2023) and numerical simulations (Huang, Shin & Sung 2007; Zhang *et al.* 2020*b*) indicate that the onset and evolution of monami are predominantly governed by 2-D shear-layer instabilities, making 2-D blade models effective for capturing the essential flow–vegetation coupling mechanisms. O'Connor & Revell (2019) investigated coupled interactions between large arrays of 2-D slender blades in open-channel flow, identifying three distinct motion modes (static, regular waving and irregular waving) primarily driven by the flow. Ni *et al.* (2025) simulated the evolution of large-scale vortices above the vegetation canopy in a 2-D laminar flow, and found that the characteristics of vegetation swaying vary synchronously with those of large-scale vortices. Furthermore, turbulent flow over the vegetation canopy has also been studied to explore the interaction between multi-scale vortical structures and coherent motions of vegetation (Tschisgale *et al.* 2021; He, Liu & Shen 2022; Wang *et al.* 2022*a*,*b*; Foggi Rota *et al.* 2024).

While the hydrodynamics of near-wall swimming and the flow-induced motion of aquatic vegetation have been extensively studied in isolation, their bidirectional coupling remains poorly understood. On the one hand, fish swimming acts as a source of flow perturbation that inevitably modulates seagrass motion. On the other hand, vegetation response not only serves as an indicator of the swimmer's locomotion, but also reciprocally affects the swimmer's propulsive performance (Dibble, Killgore & Harrel 1996). Therefore, the present study aims to investigate the dynamic interaction between a self-propelled plate (representing a flatfish-like swimmer) and multiple wall-mounted compliant blades (representing aquatic vegetation), mimicking the scenario of a fish swimming over the vegetation canopy. Specifically, this study seeks to address the following two fundamental questions. First, how does the presence of compliant blades modify the propulsive performance of a self-propelled plate near the wall? Second, how does the flapping motion of the plate excite and organise the vibration response of the compliant blade array? These investigations are intended to advance the understanding of the physical mechanisms underlying the complex fluid–structure interaction between fish and their surrounding environment, thereby providing insights into the design of bio-inspired underwater vehicles and flow sensing techniques.

The remainder of the paper is organised as follows. Section 2.1 establishes the physical model and presents the mathematical formulations, while numerical methods and validation are presented in § 2.2. Section 3 presents the results, including the time-dependent flow (§ 3.1), propulsive performance of the self-propelled plate (§ 3.2), motion of the compliant blades (§ 3.3), and resonance between the plate and the blades (§ 3.4). The key findings are summarised in § 4.

2. Methodology

2.1. *Problem set-up and governing equations*

We consider a system consisting of a self-propelled flexible plate swimming above an array of wall-mounted compliant blades, as shown in figure 1. The plate and blades are

https://doi.org/10.1017/jfm.2026.11712 Published online by Cambridge University Press

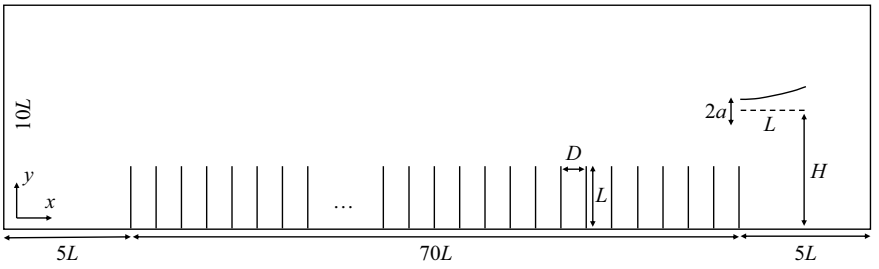


Figure 1. Schematic diagram for the self-propelled plate moving above an array of wall-mounted compliant blades.

immersed in an initially stationary viscous incompressible fluid. The self-propelled plate, with length L, exhibits a zero tangential angle and a prescribed heaving motion at its leading edge. The vertical position of the leading edge, denoted as y_l, is given by

$$y_l(t) = a\sin(2\pi t/T + \pi) + H, \tag{2.1}$$

where a is the heaving amplitude, T is the period of the heaving motion, and H is the average height of the plate above the bottom wall (where $y = 0$). The compliant blades, initially mounted vertically on the bottom wall, have uniform height L, constant spacing D, and total number N. Additionally, we assume that the thicknesses of both the plate and the blade are negligibly small.

In the system, the fluid motion is governed by the incompressible Navier–Stokes equations and the continuity equation as

$$\frac{\partial \boldsymbol{u}}{\partial t} + \boldsymbol{u}\cdot\nabla\boldsymbol{u} = -\frac{1}{\rho}\nabla p + \nu\nabla^2\boldsymbol{u} + \frac{1}{\rho}\boldsymbol{f}_{IB}, \tag{2.2}$$

$$\nabla\cdot\boldsymbol{u} = 0, \tag{2.3}$$

where $\boldsymbol{u}$ is the fluid velocity, p is the static pressure, ρ is the fluid density, and ν is the kinematic viscosity. Here, $\boldsymbol{f}_{IB}$ is the volume force introduced in the immersed boundary method. The velocity is set to zero on the four boundaries of the computational domain, and a no-slip boundary condition is applied to the plate and blades. The flow is initially stationary throughout the computational domain.

Following the approach of Connell & Yue (2007), Hua, Zhu & Lu (2013) and Peng *et al.* (2022), the self-propelled plate and compliant blades are modelled as a thin elastic beam undergoing large deformation. The governing equation for the beam is given by

$$m\frac{\partial^2\boldsymbol{X}}{\partial t^2} - Eh\frac{\partial}{\partial s}\left[\left(1 - \left|\frac{\partial\boldsymbol{X}}{\partial s}\right|^{-1}\right)\frac{\partial\boldsymbol{X}}{\partial s}\right] + EI\frac{\partial^4\boldsymbol{X}}{\partial s^4} = \boldsymbol{F}_{IB}. \tag{2.4}$$

Here, $\boldsymbol{X}(s,t) = X(s,t)\,\boldsymbol{e}_x + Y(s,t)\,\boldsymbol{e}_y$ denotes the position vector of the Lagrangian point on the beam, where s is the initial arc length measured from the leading edge of the plate or the root of the blade, m is the mass per unit length, Eh is the stretching rigidity, EI is the bending rigidity, and $\boldsymbol{F}_{IB}$ is the Lagrangian force exerted by the surrounding fluid on the plate or blades. To distinguish different solid structures, the subscript p is added to denote parameters related to the plate, whereas the subscript b or bi is adopted for parameters of the wall-mounted blade array or the ith individual blade. Parameters without a subscript apply to all solid structures.

https://doi.org/10.1017/jfm.2026.11712 Published online by Cambridge University Press

The boundary conditions at the leading edge of the self-propelled plate are given by

$$\left.\frac{\partial X_p}{\partial s}\right|_{s=0} = 1, \quad \left.\frac{\partial Y_p}{\partial s}\right|_{s=0} = 0, \quad Y_p(0,t) = y_l(t). \tag{2.5}$$

Meanwhile, the boundary conditions at the root of the ith blade are given by

$$\left.\frac{\partial X_{bi}}{\partial s}\right|_{s=0} = 0, \quad \left.\frac{\partial Y_{bi}}{\partial s}\right|_{s=0} = 1, \quad X_{bi}(0,t) = -iD, \quad Y_{bi}(0,t) = 0. \tag{2.6}$$

At the free ends of the plate and blades, the following boundary conditions are applied:

$$\left[Eh\left(1 - \left|\frac{\partial \boldsymbol{X}}{\partial s}\right|^{-1}\right)\frac{\partial \boldsymbol{X}}{\partial s} - EI\frac{\partial^3 \boldsymbol{X}}{\partial s^3}\right]_{s=L} = \boldsymbol{0}, \quad \left.\frac{\partial^2 \boldsymbol{X}}{\partial s^2}\right|_{s=L} = \boldsymbol{0}. \tag{2.7}$$

At time $t = 0$, the leading edge of the plate is located at $X_p(0,0) = 0$, and the plate is placed horizontally with $Y_p(s,0) = H$. For $t > 0$, $X_p(0,t)$ is determined by fluid–structure interaction.

Following the normalisation convention established in Lin, Wu & Zhang (2021) and Liu, Liu & Huang (2022), the fluid density ρ, plate length L, and velocity $U_{ref} = 100\nu/L$ are chosen to non-dimensionalise the above equations. The dimensionless parameters are defined as

$$S = \frac{Eh}{\rho U_{ref}^2 L}, \; K = \frac{EI}{\rho U_{ref}^2 L^3}, \; \rho^* = \frac{m}{\rho L}, \; f^* = \frac{L}{TU_{ref}}, \; A_L = \frac{2a}{L}, \; H_L = \frac{H}{L}, \; D_L = \frac{D}{L}. \tag{2.8}$$

Here, S is the dimensionless stretching stiffness, K is the dimensionless bending stiffness, and ρ^* is the dimensionless mass ratio of the solid structure. Additionally, f^* is the dimensionless flapping frequency of the plate, A_L is the dimensionless peak-to-peak heaving amplitude of the plate, H_L is the dimensionless vertical distance between the bottom wall and the plate, and D_L is the dimensionless blade spacing. The dimensionless governing equations and boundary conditions, derived using the aforementioned dimensionless parameters, are provided in Appendix A.

The nominal Reynolds number based on U_{ref} and L is 100. Although this Reynolds number is introduced primarily for non-dimensionalisation, it also sets the characteristic flow regime considered in the present study. Specifically, juvenile flatfish are benthic and can have body lengths as small as 4.1 mm (Osse & Van den Boogaart 1997), for which the Reynolds number based on typical swimming velocities falls within the same order of magnitude. It should be noted that this nominal Reynolds number does not uniquely characterise the flow physics in the self-propelled motion. More physically relevant Reynolds numbers, such as the flapping Reynolds number and the propulsive Reynolds number, are therefore introduced and discussed in the subsequent sections.

2.2. *Numerical methods and validation*

The Navier–Stokes equations are solved numerically via the lattice Boltzmann method with a D2Q9 velocity model (Chen & Doolen 1998). The deformation and motion of the plate and blades are solved via a finite element method in the Lagrangian coordinate (Doyle 2001). The immersed boundary method is used to couple the two solvers (Peskin 2002; Mittal & Iaccarino 2005). In the immersed boundary method, the Lagrangian force exerted on the solid structure is computed by the penalty function method (Goldstein,

https://doi.org/10.1017/jfm.2026.11712 Published online by Cambridge University Press

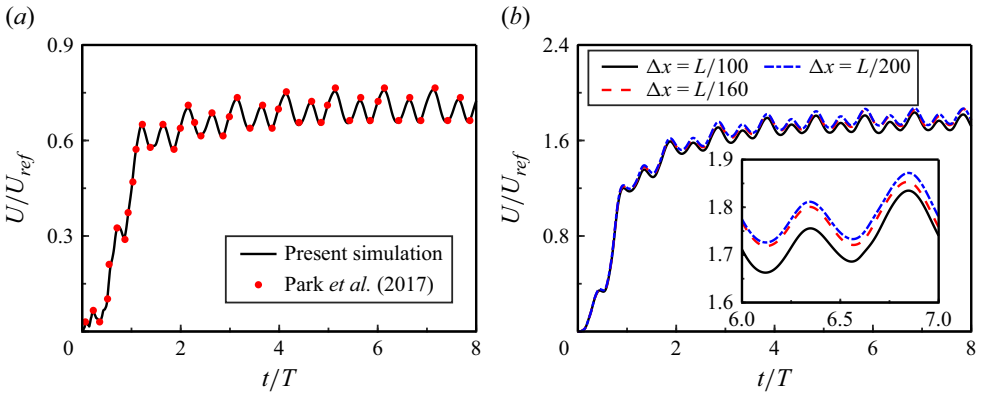


Figure 2. (*a*) Comparison of present results with previous data (Park *et al.* 2017) for the time-dependent centre-point velocity of the self-propelled plate near a smooth wall. (*b*) The time histories of the propulsive velocity of the self-propelled plate above compliant blades for different grid resolutions.

Handler & Sirovich 1993):

$$\boldsymbol{F}_{IB}(s,t) = \alpha \int_0^t \left[\boldsymbol{V}_f(s,t') - \boldsymbol{V}(s,t')\right] \mathrm{d}t' + \beta\left[\boldsymbol{V}_f(s,t) - \boldsymbol{V}(s,t)\right], \tag{2.9}$$

where α and β are free parameters selected based on previous studies (Gao & Lu 2008; Tian *et al.* 2011; Hua *et al.* 2013), $\boldsymbol{V} = \partial \boldsymbol{X}(s,t)/\partial t$ is the velocity of the Lagrangian point, and $\boldsymbol{V}_f$ is the fluid velocity at the structure position, obtained by interpolation as

$$\boldsymbol{V}_f(s,t) = \iint_{\Omega} \boldsymbol{u}(\boldsymbol{x},t)\, \delta(\boldsymbol{x} - \boldsymbol{X}(s,t))\, \mathrm{d}\boldsymbol{x}. \tag{2.10}$$

Here, Ω denotes the entire computational domain, and $\delta(\boldsymbol{x})$ is the smoothed Dirac delta function in 2-D space, given by

$$\delta(\boldsymbol{x}) = \frac{1}{\Delta x^2}\phi\left(\frac{x}{\Delta x}\right)\phi\left(\frac{y}{\Delta x}\right), \tag{2.11}$$

where Δx is the uniform grid size, and $\phi(x)$ is defined as

$$\phi(x) = \begin{cases} \left(3 - 2|x| + \sqrt{1 + 4|x| - 4|x|^2}\right)/8, & |x| < 1, \\ \left(5 - 2|x| + \sqrt{-7 + 12|x| - 4|x|^2}\right)/8, & 1 \leqslant |x| < 2, \\ 0, & |x| \geqslant 2. \end{cases} \tag{2.12}$$

The Eulerian volume force is calculated as

$$\boldsymbol{f}_{IB}(\boldsymbol{x},t) = -\int_{\Gamma} \boldsymbol{F}_{IB}(s,t)\, \delta(\boldsymbol{x} - \boldsymbol{X}(s,t))\, \mathrm{d}s, \tag{2.13}$$

where Γ denotes the integration path along the plate and blades. The interaction forces $\boldsymbol{F}_{IB}(s,t)$ and $\boldsymbol{f}_{IB}(\boldsymbol{x},t)$ obtained from (2.9) and (2.13) are used in (2.4) and (2.2), respectively.

This numerical method has been successfully applied to a wide range of studies (Hua *et al.* 2013; Tang *et al.* 2016; Peng, Huang & Lu 2018; Zhang *et al.* 2020*a*, 2026). To further validate the numerical set-up, a self-propelled plate near a smooth wall is simulated. Figure 2(*a*) shows the time histories of the velocity at the middle point of the plate. The present results agree well with those in Park *et al.* (2017).

https://doi.org/10.1017/jfm.2026.11712 Published online by Cambridge University Press

ρ^*	S_p	S_b	K_p	K_b	f^*	A_L	H_L	D_L
1.0	1000	1000	2.75–5.00	0.25–30	0.38–0.64	0.1–0.5	1.5–2.0	0.25–1.0

Table 1. The ranges of dimensionless parameters considered in the present study.

Based on convergence studies across different computational domains, the computational domain is chosen as $x \in [-75L, 5L]$, $y \in [0, 10L]$, which is sufficiently large to neglect the blockage effect. The compliant blades are equally spaced over the range $x \in [-70L, 0]$. A grid convergence study is performed with the key parameters $f^* = 0.64$, $A_L = 0.5$, $D_L = 0.5$, $H_L = 1.5$, $K_p = 3.5$, $K_b = 3.0$, $S_p = S_b = 1000$, and the results are presented in figure 2(*b*). Here, the instantaneous propulsive velocity U of the self-propelled plate is defined as

$$U = -\frac{1}{L}\int_0^L \frac{\partial X(s,t)}{\partial t}\,\mathrm{d}s, \tag{2.14}$$

where a negative sign is introduced because the plate moves in the negative x-direction. For the three tested grid resolutions, the propulsive velocity curves of $\Delta x = L/160$ and $\Delta x = L/200$ are nearly identical. Therefore, the grid spacing $\Delta x = L/160$ and time step $\Delta t = T/10\,000$ are employed for all subsequent simulations.

3. Results

The ranges of dimensionless parameters considered in the present study are summarised in table 1. The mass ratio ρ^* is set to 1. A large stretching stiffness ($S_p = S_b = 1000$) is employed for both the self-propelled plate and compliant blades to eliminate the influence of stretching deformation. The bending stiffness of the plate K_p is varied from 2.75 to 5.00, including the value of 3.5 that corresponds to the maximum propulsive velocity at flapping amplitude $A_L = 0.5$ in an unbounded domain (Luo, Gao & Lu 2023). The range $f^* \in [1.2/\pi, 2/\pi]$, i.e. [0.38, 0.64], is chosen such that the Reynolds number defined by the maximum heaving velocity of the plate's leading edge with $A_L = 0.5$ falls within [60, 100], consistent with the order of magnitude in Liu *et al.* (2022). The vertical distance between the plate and the wall H_L ranges from 1.5 to 2.0, and the spacing between adjacent blades D_L ranges from 0.25 to 1.0, ensuring substantial mutual interactions while avoiding direct solid–solid contact. Accordingly, all conclusions drawn in this study are restricted to the non-contact parameter range considered here.

3.1. *Time-dependent flow*

A series of simulations is performed at flapping frequency $f^* = 0.64$ for the self-propelled plate, considering different blade spacing D_L and vertical plate-wall distance H_L. The motion of the plate reaches a periodic state for $t/T \geqslant 15$. Figure 3 presents the dimensionless vorticity fields ($\omega_z^* = \omega_z L/U_{ref}$) at $t/T = 19.75$, corresponding to the instant at which the leading edge of the plate reaches its maximum vertical displacement (see supplementary movie 1 for the vorticity evolution, available at https://doi.org/10.1017/jfm.2026.11712.). For comparison, three reference cases are also presented. The first is an unbounded-domain case with $D_L \to \infty$ and $H_L \to \infty$, shown in figure 3(*a*). The other two are smooth-wall cases with $D_L \to \infty$: smooth-wall case 2 (SW2), with $H_L = 1.5$, shown in figure 3(*b*); and smooth-wall case 1 (SW1), with $H_L = 0.5$, shown in figure 3(*f*). Specifically, SW1 is equivalent to raising the smooth wall to the tips of the undeformed blades.

https://doi.org/10.1017/jfm.2026.11712 Published online by Cambridge University Press

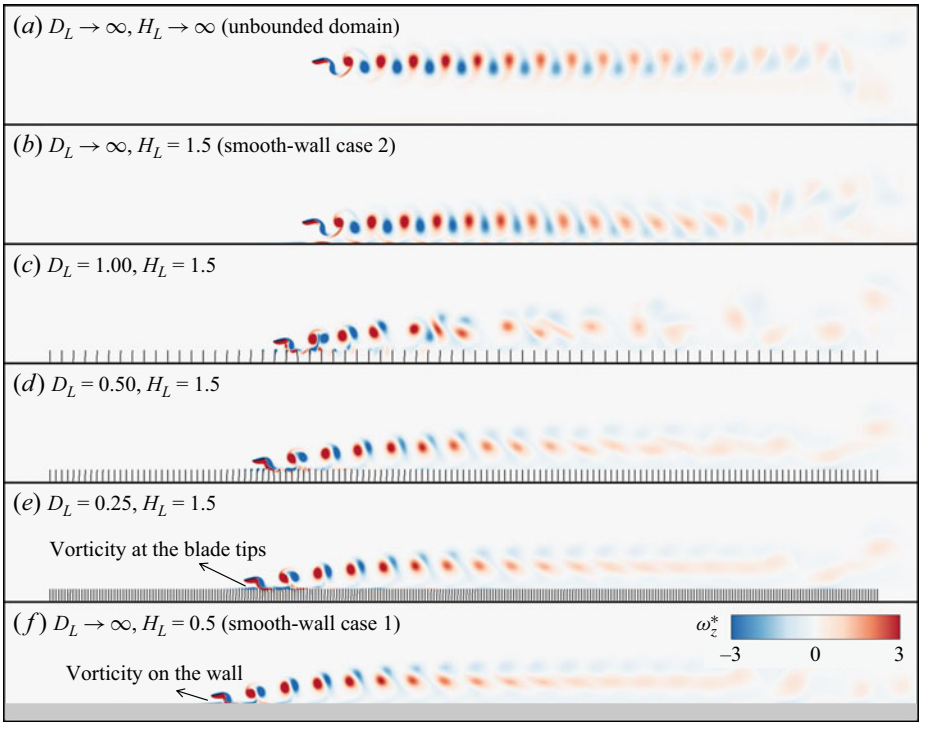


Figure 3. The dimensionless vorticity fields at $t/T = 19.75$. The leading edge of the plate is at its highest vertical displacement: (*a*) unbounded domain ($D_L \to \infty$, $H_L \to \infty$); (*b*) smooth wall ($D_L \to \infty$, $H_L = 1.5$); (*c*) compliant blade array with $D_L = 1.00$, $H_L = 1.5$; (*d*) compliant blade array with $D_L = 0.50$, $H_L = 1.5$; (*e*) compliant blade array with $D_L = 0.25$, $H_L = 1.5$; (*f*) smooth wall with a reduced plate–wall distance, $D_L \to \infty$, $H_L = 0.5$. Grey area denotes solid wall. Here, $f^* = 0.64$, $A_L = 0.5$, $K_p = 3.5$, $K_b = 3.0$. See supplementary movie 1 for the vorticity evolution.

From figure 3(*a*) to figure 3(*f*), the distance travelled by the self-propelled plate increases monotonically, indicating that reducing either the vertical plate–wall distance H_L or the blade spacing D_L enhances the propulsive velocity of the plate. Notably, the discrepancy between the case in the unbounded domain and the case SW2 is negligible, and both cases exhibit the classical reverse Bénard–von Kármán vortex street in the near wake. By contrast, the other cases exhibit a vortex-pair wake, which initially deflects upwards before gradually transitioning to a horizontal orientation. This upward-deflected vortex wake, which is also observed in previous studies with a smooth wall (Quinn *et al.* 2014; Dai *et al.* 2016; Tang *et al.* 2016; Park *et al.* 2017; Zhang *et al.* 2017), arises because the positive vortex generated during the downward stroke of the plate is stronger. In particular, for the case where the blade spacing equals the plate length ($D_L = 1.00$), the far wake exhibits an irregular spatial arrangement of vortices. Beneath the plate, a layer of negative vorticity forms at the blade tips or on the smooth wall due to the plate's flapping motion, as indicated by the black arrow in figures 3(*e*) and 3(*f*); downstream of the vortex pair shed during the previous period, this wall-interaction vorticity becomes negligible.

The trailing-edge displacement of the flexible plate is a representative response of the fluid–structure system and is closely related to its propulsive performance (Smits 2019). To clarify how the compliant blades modify the plate deformation, figure 4(*a*) presents the time-dependent vertical displacements of the leading edge y_l and trailing edge y_t of the self-propelled plate for the case with $D_L = 0.25$, $H_L = 1.5$ and the case with

https://doi.org/10.1017/jfm.2026.11712 Published online by Cambridge University Press

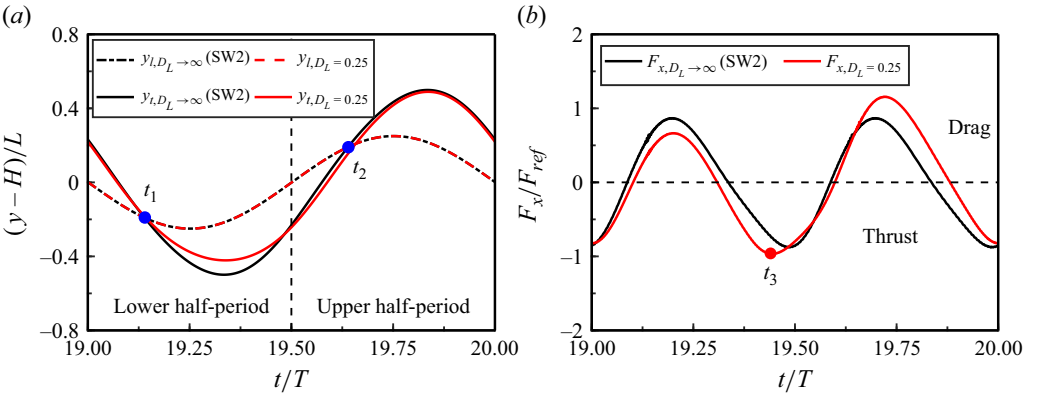


Figure 4. (*a*) Time histories of the vertical displacements of the leading edge y_l and trailing edge y_t of the self-propelled plate over one period. Blue dots indicate the instants $t_1 = 19.14T$ and $t_2 = 19.64T$ at which the plate is oriented horizontally. (*b*) Time histories of the horizontal force F_x acting on the plate. Red dot denotes the instant $t_3 = 19.44T$ corresponding to the maximum thrust in the case with $D_L = 0.25$. Here, $f^* = 0.64$, $A_L = 0.5$, $H_L = 1.5$, $K_p = 3.5$, $K_b = 3.0$.

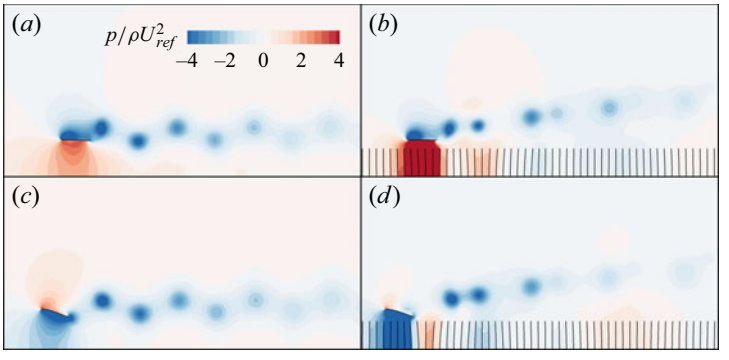


Figure 5. The dimensionless pressure fields at (*a,b*) $t_1 = 19.14T$ and (*c,d*) $t_3 = 19.44T$ for two typical cases: (*a,c*) case with $D_L \to \infty$, $H_L = 1.5$ (SW2), (*b,d*) case with $D_L = 0.25$, $H_L = 1.5$. Here, $f^* = 0.64$, $A_L = 0.5$, $K_p = 3.5$, $K_b = 3.0$.

$D_L \to \infty$, $H_L = 1.5$ (SW2). After the leading edge passes its minimum vertical displacement at $t/T = 19.25$ and starts moving upwards, the trailing edge continues moving downwards due to inertia; similarly, the trailing edge keeps going upwards after the leading edge passes its maximum displacement at $t/T = 19.75$. Consequently, the trailing edge exhibits a larger oscillation amplitude than the leading edge, with phase lag approximately $0.1T$ relative to the latter. At the instants $t_1 = 19.14T$ and $t_2 = 19.64T$ (marked with blue dots), corresponding to $y_l/L = -0.19$ and 0.19, respectively, the trailing edge and leading edge are at the same vertical position, and the plate is oriented horizontally. For convenience, the lower half-period is defined as $t/T \in (19, 19.5]$, during which the leading edge is below its average height H, while the upper half-period is defined as $t/T \in (19.5, 20]$, during which the leading edge is above its average height. Compared to case SW2, the trailing-edge displacement of the plate in the case with $D_L = 0.25$, $H_L = 1.5$ remains largely unchanged during the upper half-period, but is notably suppressed after t_1 in the lower half-period due to the enhanced pressure beneath the plate. This is illustrated in figures 5(*a*) and 5(*b*), which present the dimensionless pressure fields of the two cases at t_1. As a result, the symmetry of the plate deformation between the lower and upper half-periods is broken.

https://doi.org/10.1017/jfm.2026.11712 Published online by Cambridge University Press

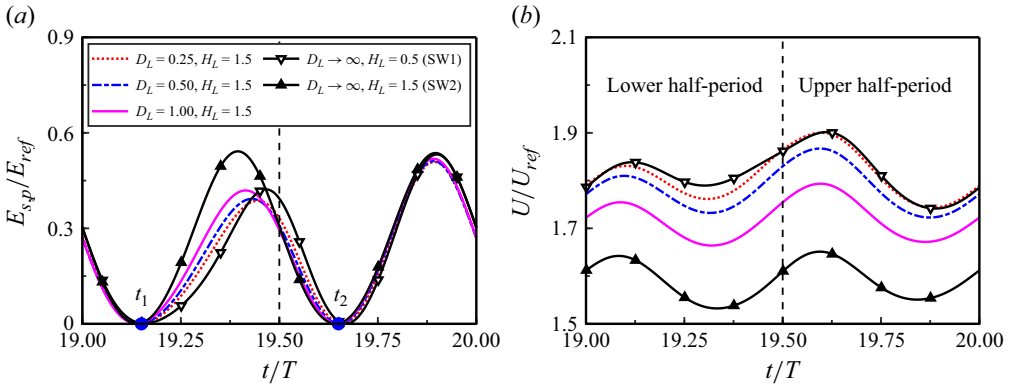


Figure 6. (*a*) Time histories of the strain energy of the self-propelled plate for different cases. (*b*) Time histories of the propulsive velocity. Blue dots indicate the instants t_1 and t_2 at which the plate is oriented horizontally. Here, $f^* = 0.64$, $A_L = 0.5$, $K_p = 3.5$, $K_b = 3.0$.

To explore the influence of compliant blades on the hydrodynamic force, the time-dependent horizontal force F_x, rescaled by $F_{ref} = \rho U_{ref}^2 L$, exerted on the self-propelled plate is shown in figure 4(*b*). The maximum thrust is achieved when the leading edge is close to the average height ($t/T = 19$ and 19.5), while the maximum drag occurs near the minimum and maximum vertical displacements ($t/T = 19.25$ and 19.75). For the case with $D_L = 0.25$, $H_L = 1.5$, the maximum thrust occurs slightly earlier than that in case SW2, and the maximum drag occurs later than that in case SW2. In the lower half-period, although the plate exhibits reduced deformation, its thrust ($-F_x$) is dramatically enhanced by the ground effect, especially when the plate moves from the minimum vertical displacement to the average position, i.e. $t/T \in (19.25, 19.5)$. This enhancement in thrust is primarily attributed to the increased suction within the low-pressure region between the plate and the bottom wall, as illustrated in figures 5(*c*) and 5(*d*), which present the dimensionless pressure fields of the two cases at $t_3 = 19.44T$. By contrast, in the upper half-period, the drag (F_x) increases when the plate moves from its maximum vertical displacement to the average position, i.e. $t/T \in (19.75, 20)$.

To further quantify the deformation of the self-propelled plate, the time-dependent strain energy of the plate, normalised by $E_{ref} = \rho U_{ref}^2 L^2$, is presented in figure 6(*a*). The strain energy is defined as

$$E_{s,p} = \int_0^L 0.5(EI)_p \left| \frac{\partial^2 \boldsymbol{X}_p(s,t)}{\partial s^2} \right|^2 \mathrm{d}s. \tag{3.1}$$

Since $E_{s,p}$ is the integration of the square of the curvature over the entire plate, it represents the overall deformation of the plate. For all cases, $E_{s,p}$ reaches zero at almost the same instants t_1 and t_2. During the time intervals $t \in (19T, t_1)$ and $t \in (t_2, 20T)$, the bottom wall or blade array has a negligible effect on the deformation of the plate; in the remaining period, the ground effect strongly suppresses the strain energy of the plate for $t \in (t_1, 19.42T)$, whereas it slightly enhances the strain energy for $t \in (19.42T, t_2)$.

The time-dependent propulsive velocity of the self-propelled plate, defined by (2.14), is presented in figure 6(*b*). Compared with the smooth-wall case SW2, the compliant blades increase the propulsive velocity of the plate over the entire period, and the velocity enhancement intensifies as the blade spacing decreases. Furthermore, the local maximum velocity during the upper half-period is larger than that during the lower half-period, and

https://doi.org/10.1017/jfm.2026.11712 Published online by Cambridge University Press

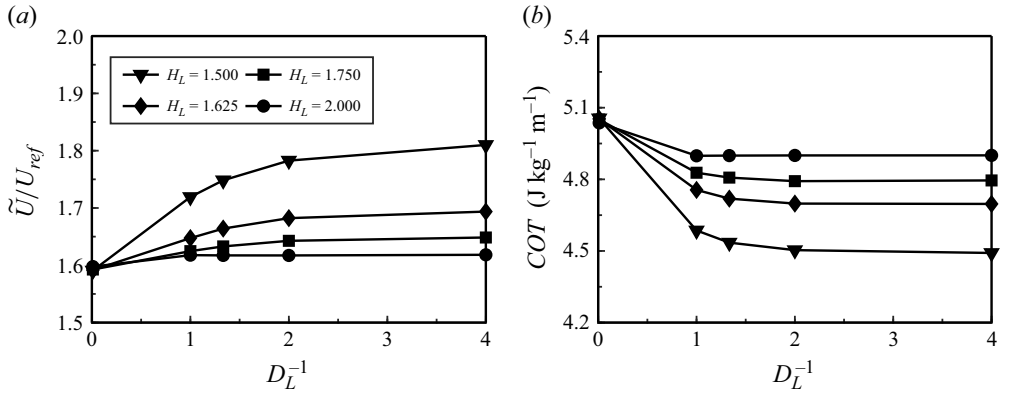


Figure 7. (*a*) The average propulsive velocity and (*b*) the cost of transport of the self-propelled plate as functions of D_L^{-1} across different H_L. Here, $f^* = 0.64$, $A_L = 0.5$, $K_p = 3.5$, $K_b = 3.0$.

the local minimum velocity during the upper half-period is smaller than that during the lower half-period. These results indicate that the compliant blades break the symmetry of the plate's motion. After the instant t_2 in the upper half-period, the instantaneous propulsive velocity of the plate is enhanced, whereas its deformation remains largely unchanged; as a result, this leads to an increase in the drag exerted on the plate, as evidenced by figure 4(*b*).

3.2. *Propulsive performance and scaling law*

For $t/T \geqslant 15$, the motion of the self-propelled plate is already independent of its initial conditions, and the notation $\widetilde{(\cdot)}$ is employed to denote the time averaging over the interval $t \in [15T, 25T]$. The average propulsive velocity $\widetilde{U}$ and average power consumption $\widetilde{P}$ are defined as

$$\widetilde{U} = \frac{1}{10T}\int_{15T}^{25T} U \,\mathrm{d}t, \quad \widetilde{P} = \frac{1}{10T}\int_{15T}^{25T}\int_{0}^{L} -\boldsymbol{\tau}(s,t)\cdot\frac{\partial \boldsymbol{X}(s,t)}{\partial t}\,\mathrm{d}s\,\mathrm{d}t, \tag{3.2}$$

where $\boldsymbol{\tau}$ denotes the fluid stress exerted on the plate. It should be noted that $\widetilde{P}$, representing the average power delivered by the plate to the fluid, is equal to the average power supplied by the external force acting at the leading edge of the plate, because the net change of the total mechanical energy of the plate is zero from $t = 15T$ to $t = 25T$. Furthermore, the cost of transport (COT), a parameter quantifying the energy consumption per unit mass and transport distance, is defined as

$$COT = \frac{\widetilde{P}}{mL\widetilde{U}}. \tag{3.3}$$

Here, mL is the mass of the plate.

Figure 7 presents $\widetilde{U}$ and COT of the self-propelled plate as functions of the blade spacing. Here, the reciprocal of the blade spacing, D_L^{-1}, is employed, and $D_L^{-1} = 0$ corresponds to the smooth-wall cases. For the smooth-wall cases, $\widetilde{U}$ and COT are insensitive to H_L over the range 1.5–2.0, indicating that the ground effect provided by the smooth wall alone is negligible. By contrast, in the presence of compliant blades, $\widetilde{U}$ increases and COT decreases with increasing D_L^{-1}, indicating enhancements in both propulsion velocity and energy efficiency. For $D_L^{-1} \geqslant 2$, $\widetilde{U}$ and COT tend to plateau. Notably, the enhancements in propulsive velocity and energy efficiency are more

https://doi.org/10.1017/jfm.2026.11712 Published online by Cambridge University Press

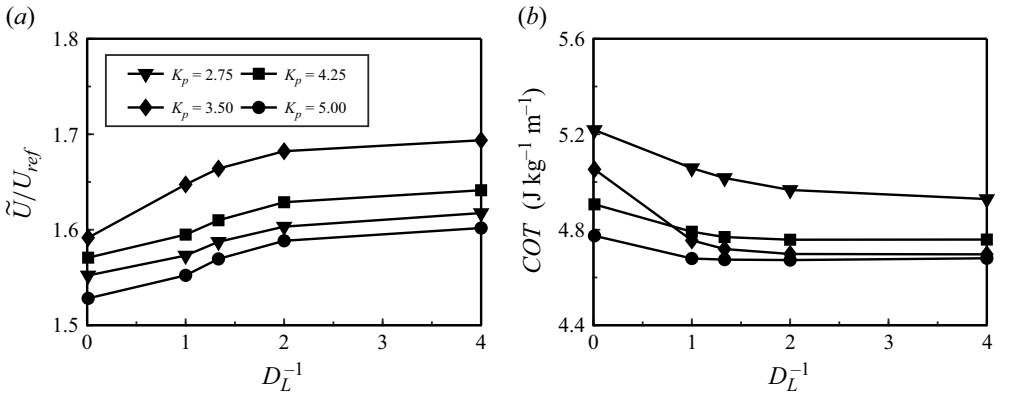


Figure 8. (*a*) The average propulsive velocity and (*b*) the cost of transport of the self-propelled plate as functions of D_L^{-1} across different K_p. Here, $f^* = 0.64$, $A_L = 0.5$, $H_L = 1.625$, $K_b = 3.0$.

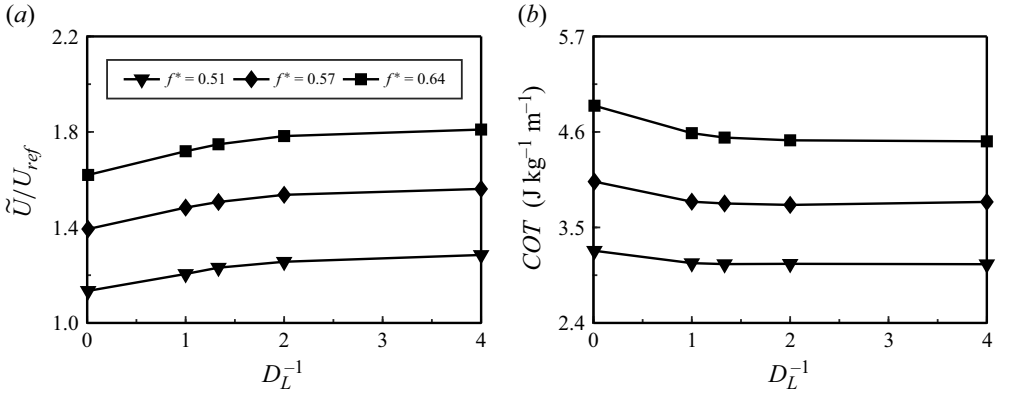


Figure 9. (*a*) The average propulsive velocity and (*b*) the cost of transport of the self-propelled plate as functions of D_L^{-1} across different f^*. Here, $H_L = 1.5$, $A_L = 0.5$, $K_p = 3.5$, $K_b = 3.0$.

pronounced when H_L is decreased from 1.625 to 1.5 than when it is decreased from 2.0 to 1.625, revealing a nonlinear dependence of the ground effect on H_L. Further reducing H_L may lead to direct contact between the plate and blades; this situation is not considered in the present study.

Figure 8 shows the effect of the plate bending stiffness K_p on the propulsive performance. Here, H_L is set to 1.625 so that the ground effect remains significant. For all values of K_p considered, increasing D_L^{-1} leads to a higher $\widetilde{U}$ and a lower COT, indicating simultaneous improvements in swimming speed and transport efficiency. However, the extent of this improvement depends on K_p. In particular, the case $K_p = 3.5$, which yields the highest $\widetilde{U}$ overall, also exhibits the most pronounced enhancement as D_L^{-1} increases. As a result, although its COT is higher than that of the $K_p = 4.25$ case at $D_L^{-1} = 0$, it becomes lower when $D_L^{-1} \geqslant 1$. Since $K_p = 3.5$ provides relatively good overall propulsive performance, it is adopted in the remainder of the study.

The effect of the flapping frequency f^* of the self-propelled plate on its propulsive performance is further examined. As shown in figure 9, across all f^*, $\widetilde{U}$ and COT exhibit the same trends of variation: $\widetilde{U}$ increases monotonically and COT decreases monotonically with increasing D_L^{-1}. As f^* increases, both $\widetilde{U}$ and COT increase. Specifically, with

https://doi.org/10.1017/jfm.2026.11712 Published online by Cambridge University Press

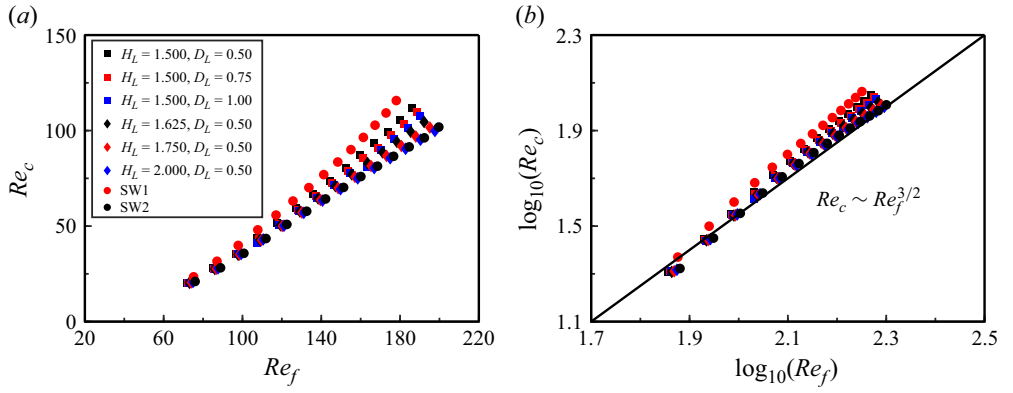


Figure 10. The relationship between the propulsive Reynolds number Re_c and the flapping Reynolds number Re_f in (*a*) linear coordinates and (*b*) logarithmic coordinates. Here, $f^* = 0.64$, $K_p = 3.5$, $K_b = 3.0$, $0.1 \leqslant A_L \leqslant 0.5$.

f^* increasing from 0.51 to 0.64, $\widetilde{U}$ increases by approximately 0.34 (from 0.51 to 0.57) and 0.24 (from 0.57 to 0.64), while *COT* increases by 0.72 and 0.77, respectively. These results indicate that a higher flapping frequency of the plate enhances its propulsive velocity at the cost of decreased energy efficiency.

Universal scaling laws have long been a core research focus in the study of biological and bio-inspired propulsive systems (Gazzola, Argentina & Mahadevan 2014; Floryan *et al.* 2017; Ayancik *et al.* 2019; Lin *et al.* 2021; Liu *et al.* 2022). To investigate the scaling law for the self-propelled plate near the blade-covered wall, figure 10(*a*) presents the propulsive Reynolds number $Re_c = \widetilde{U} L/\nu$ as a function of the flapping Reynolds number Re_f for different blade spacing D_L and vertical plate–wall distance H_L. Here, the varying $\widetilde{U}$ is achieved by changing the heaving amplitude of the plate leading edge in the range $0.1 \leq A_L \leq 0.5$. Here, Re_f is defined using the flapping amplitude a_t at the trailing edge of the plate as $Re_f = 2\pi T^{-1} a_t L/\nu$ (Gazzola *et al.* 2014; Liu *et al.* 2022), in which a_t is defined as

$$a_t = 0.5[\max(y_t) - \min(y_t)]. \tag{3.4}$$

For fixed H_L and D_L, Re_c (an indicator of propulsive velocity) increases monotonically with Re_f at a rate steeper than linear growth. Furthermore, for a given Re_f value, Re_c increases with decreasing H_L and D_L. The logarithmic plot (figure 10*b*) further reveals an approximate power-law relationship between Re_c and Re_f, where the corresponding power-law exponent increases as H_L and D_L decrease.

For the plate moving above a smooth wall at $H_L = 1.5$ (SW2), where the ground effect is negligible, the data follow the scaling law $Re_c \sim Re_f^{3/2}$ derived by Liu *et al.* (2022). This scaling law can be interpreted as follows. The thrust scaling for a self-propelled slender body follows $F_{thrust} \sim (a_t/T)^2$, as established by Gazzola *et al.* (2014) and Quinn *et al.* (2014). The drag scaling for the self-propelled plate is $F_{drag} \sim \widetilde{U}^{4/3}$, as thoroughly validated by Liu *et al.* (2022). By balancing the thrust and drag, we have $\widetilde{U}^{4/3} \sim (a_t/T)^2$, i.e. $\widetilde{U} \sim (a_t/T)^{3/2}$. Based on the definitions of Re_c and Re_f, this relationship can be further written as $Re_c \sim Re_f^{3/2}$.

When the ground effect becomes significant, the trailing-edge displacement of the plate becomes asymmetric between the upper and lower half-periods. To distinguish the two half-periods, the maximum trailing-edge displacements during the upper and lower

https://doi.org/10.1017/jfm.2026.11712 Published online by Cambridge University Press

half-periods are defined as

$$a_{upper} = \max(y_t - H), \quad a_{lower} = \max(H - y_t). \tag{3.5}$$

In the upper half-period, because the plate deformation remains largely unchanged, the thrust and drag obey the same scaling laws as in the unbounded domain:

$$F_{thrust,upper} \sim (a_{upper}/T)^2, \quad F_{drag,upper} \sim \widetilde{U}^{4/3}. \tag{3.6}$$

In the lower half-period, when the trailing edge moves downwards after t_1, the decrease in a_{lower} is attributed to the enhanced vertical pressure force, which is generated by the high pressure between the plate and wall, as shown in figure 5(*b*). Given the approximate symmetry of the plate motion during its approach towards and recession from the wall, it is reasonable to assume that the ground effect exerts an equivalent amplifying influence on both the positive and negative pressures beneath the plate. Specifically, the negative pressure induced during upward motion and the positive pressure induced during downward motion are both amplified by a factor δ. Therefore, the maximum trailing-edge displacement for the lower half-period is reduced by a factor δ, i.e.

$$a_{lower} = a_{upper}/\delta, \tag{3.7}$$

whereas the thrust generated by the plate is enhanced by a factor δ, i.e.

$$F_{thrust,lower} \sim \delta\, F_{thrust,upper}. \tag{3.8}$$

In addition, since the drag is proportional to the effective frontal area of the plate, which scales linearly with the trailing-edge displacement, we have

$$F_{drag,lower} \sim \frac{a_{lower}\, F_{drag,upper}}{a_{upper}} \sim \frac{F_{drag,upper}}{\delta}. \tag{3.9}$$

By taking the average of the two half-periods, the average thrust of the self-propelled plate over a full period scales as

$$F_{thrust} \sim 0.5(F_{thrust,\,upper} + F_{thrust,\,lower}) \sim 0.5(1+\delta)\big(a_{upper}/T\big)^2. \tag{3.10}$$

Similarly, the drag over a full period scales as

$$F_{drag} \sim 0.5(F_{drag,\,upper} + F_{drag,\,lower}) \sim 0.5(1+1/\delta)\widetilde{U}^{4/3}. \tag{3.11}$$

By balancing the average thrust and drag over a full period, $F_{thrust} \sim F_{drag}$, we have

$$0.5(1+1/\delta)\widetilde{U}^{4/3} \sim 0.5(1+\delta)\big(a_{upper}/T\big)^2 \quad \Rightarrow \quad \widetilde{U} \sim \big(\sqrt{\delta}\, a_{upper}/T\big)^{3/2}, \tag{3.12}$$

which can be further written as

$$Re_c \sim \big(Re_{f,\delta}\big)^{3/2}. \tag{3.13}$$

Here, the corrected flapping Reynolds number is defined as

$$Re_{f,\delta} = 2\pi T^{-1}\left(\sqrt{\delta}\, a_{upper}\right) L/\nu. \tag{3.14}$$

The Strouhal number $St = a_t/T\widetilde{U}$ is also widely adopted to characterise self-propulsion (Gazzola *et al.* 2014). Following the same correction strategy as for $Re_{f,\delta}$, a corrected Strouhal number St_δ is defined as

$$St_\delta = \frac{\sqrt{\delta}\, a_{upper}}{T\widetilde{U}} \sim \frac{Re_{f,\delta}}{Re_c}. \tag{3.15}$$

Using the scaling relation (3.13), the relationship between Re_c and St_δ can be derived as

$$Re_c \sim (Re_{f,\delta})^{3/2} \quad \Rightarrow \quad Re_c \sim (Re_c\, St_\delta)^{3/2} \quad \Rightarrow \quad Re_c \sim St_\delta^{-3}. \tag{3.16}$$

https://doi.org/10.1017/jfm.2026.11712 Published online by Cambridge University Press

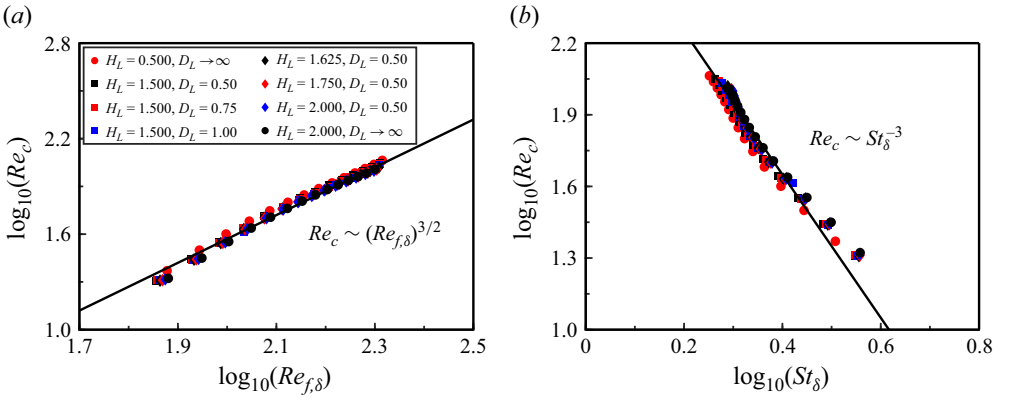


Figure 11. (*a*) Relation between the propulsive Reynolds number Re_c and the corrected flapping Reynolds number $Re_{f,\delta}$ in logarithmic coordinates. (*b*) Relation between the propulsive Reynolds number Re_c and the corrected Strouhal number St_δ in logarithmic coordinates. Here, $f^* = 0.64$, $K_p = 3.5$, $K_b = 3.0$, $0.1 \leq A_L \leq 0.5$.

The relations of Re_c with $Re_{f,\delta}$ and St_δ are displayed in figures 11(*a*) and 11(*b*), respectively. Here, a_{upper}, a_{lower} and δ are calculated *post hoc* using (3.5) and (3.7). All data points collapse onto the black solid lines given by (3.13) and (3.16), confirming the validity of the proposed scaling laws in the current Reynolds number range.

3.3. *Vibration characteristics of the wall-mounted blades*

The vibration of the wall-mounted compliant blades induced by the heaving motion of the self-propelled plate is examined under the parameter settings $A_L = 0.5$, $D_L = 0.25$, $K_p = 3.5$, $K_b = 3.0$, $H_L = 1.5$. Figure 12 presents the spatiotemporal distribution of the horizontal displacement at the blade tip, denoted by dx, with positive and negative values indicating rightward and leftward deflections, respectively. Here, the tip displacements dx of all blades in the computational domain are shown. In addition, the horizontal coordinate denotes the x-position of the corresponding blade root, and the vertical coordinate denotes the dimensionless time. The time interval $tU_{ref}/L \in [24, 40]$, corresponding to $t/T \in [15, 25]$ for $f^* = 0.64$, is selected because the entire blade array has reached a statistically periodic state.

Three distinct regimes, labelled A, B and C, are identified in figure 12, which are separated by the trajectory of the plate's leading edge and that shifted upwards by one flapping period T. In regime A, since the self-propelled plate has not yet arrived, the blades exhibit negligible vibration, except for those in the immediate upstream of the leading-edge trajectory. In regime B, as the plate passes over the blades within one flapping period, the blades experience intense excitation, leading to a sudden increase in their vibration amplitude. In regime C, after the plate has moved away, the blades exhibit free vibrations, with their amplitude gradually decaying over time due to viscous dissipation. Notably, a travelling-wave pattern exists in regime C, which propagates along the direction of plate motion at a speed significantly faster than the plate's propulsive velocity $\widetilde{U}$. This pattern is herein referred to as the forward-propagating travelling wave (FPTW), with one of its wavefronts marked by the red dashed line in the figures. The phase velocity of the FPTW is denoted by U_w. As the flapping frequency f^* of the plate increases, both $\widetilde{U}$ and U_w increase, corresponding to reduced slopes in the spatiotemporal diagrams. Meanwhile, a higher $\widetilde{U}$ enables the plate to travel a greater distance within one flapping period, thereby enlarging the spatial extent of regime B.

https://doi.org/10.1017/jfm.2026.11712 Published online by Cambridge University Press

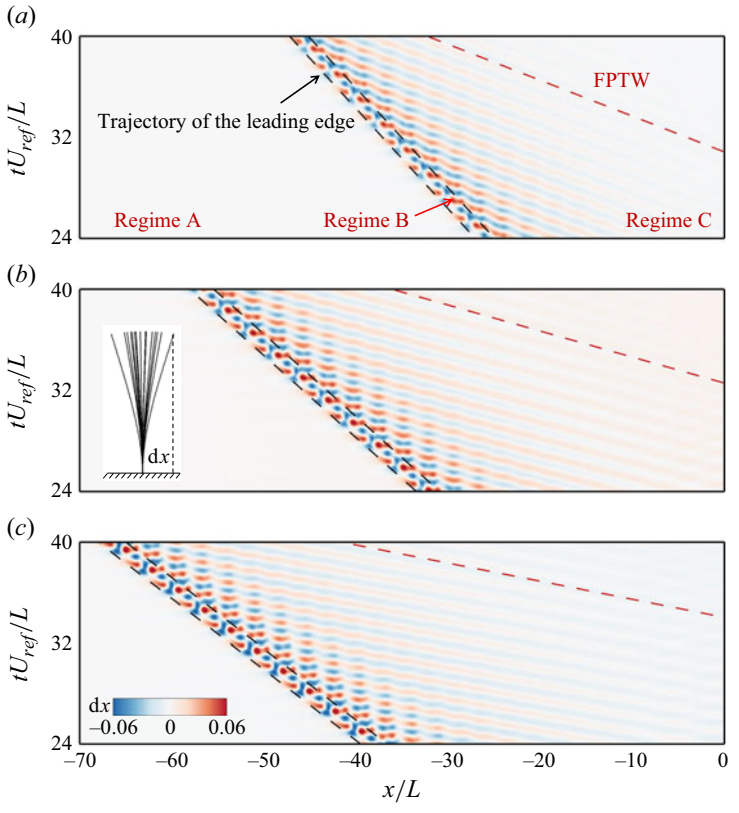


Figure 12. Spatiotemporal distribution of the horizontal displacement dx at the tips of all blades in the computational domain. The horizontal coordinate denotes the x-position of the corresponding blade root, and the vertical coordinate denotes the dimensionless time. Here, (*a*) $f^* = 0.51$, (*b*) $f^* = 0.57$, (*c*) $f^* = 0.64$. The two black dashed lines denote the trajectory of the plate leading edge and that shifted upwards by T. The red dashed line marks a wavefront of the FPTW. Here, $A_L = 0.5$, $D_L = 0.25$, $H_L = 1.5$, $K_p = 3.5$, $K_b = 3.0$.

From a spatial perspective, figure 13(*a*) presents the distribution of horizontal displacement at the blade tips at $t/T = 19.00$. In regime A, a small number of blades upstream of the leading edge of the plate are pre-excited by the plate, a phenomenon hereafter referred to as the upstream influence, leading to leftward displacements at their tips. Moreover, the tip displacements of these blades decrease monotonically as the distance from the leading edge increases. The region where the displacement exceeds 5 % of that at the plate leading edge is indicated by a red line, whose streamwise extent is approximately $3L$. By contrast, the blades in regime B exhibit a sharp increase in tip displacement over a narrow streamwise interval. In regime C, the tip displacement decays progressively with increasing distance from the plate.

From a temporal perspective, figure 13(*b*) presents the time history of the horizontal displacement at the tip of a representative blade located at $x/L = -17.25$. The vibration process is also partitioned into three regimes. In regime A, before the arrival of the leading edge of the self-propelled plate, the tip displacement exhibits slight oscillation due to the upstream influence. The most significant wave is highlighted in a red line, whose temporal extent is approximately $0.8T$. In regime B, the tip displacement increases rapidly over a short time interval, and exhibits irregular oscillations. In regime C, the tip displacement exhibits a typical underdamped free vibration, characterised by a decaying amplitude

https://doi.org/10.1017/jfm.2026.11712 Published online by Cambridge University Press

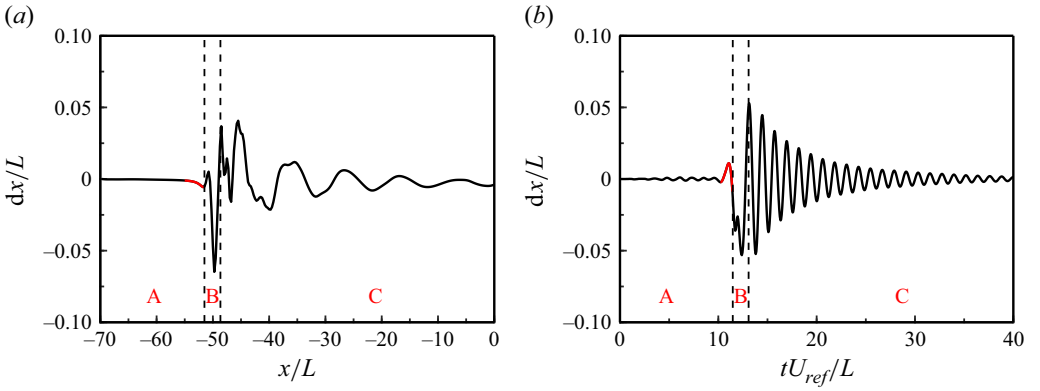


Figure 13. (*a*) Spatial distribution of horizontal displacement at the blade tips at $t/T = 19.00$. (*b*) Time history of the horizontal displacement at the tip of a representative blade located at $x/L = -17.25$. The red lines highlight regions with significant displacement in regime A. The dimensionless parameters and the definition of the black dashed lines are the same as in figure 12(*c*), i.e. $f^* = 0.64$, $A_L = 0.5$, $D_L = 0.25$, $H_L = 1.5$, $K_p = 3.5$, $K_b = 3.0$.

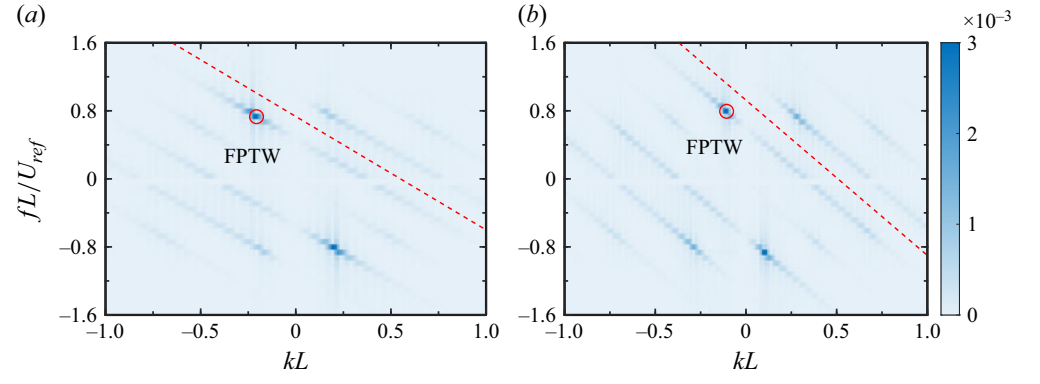


Figure 14. Spatiotemporal spectral distributions of horizontal displacements at the blade tips, for (*a*) $f^* = 0.51$, (*b*) $f^* = 0.64$. The slope of the red dashed line represents the group velocity ($U_g = -\mathrm{d}f/\mathrm{d}k$). The red circle marks the most energetic spatiotemporal frequency.

profile and dimensionless vibration frequency 0.79, which is close to its natural frequency ($f_n^{inv} L/U_{ref} = 0.73$) in inviscid fluid. Here, the natural frequency f_n^{inv} is computed by

$$f_n^{inv} = \frac{\Lambda^2}{2\pi L^2}\sqrt{\frac{EI}{m + 0.25 C_m \pi \rho L}}, \tag{3.17}$$

where $\Lambda = 1.875$ is the first positive root of the equation

$$1 + \cos\Lambda \cosh\Lambda = 0, \tag{3.18}$$

and $C_m \approx 1$ represents the added-mass effect (Van Eysden & Sader 2006; Brunetto *et al.* 2008; Xiong *et al.* 2024).

These observations reveal that the compliant blades exhibit qualitatively distinct vibration characteristics in regimes B and C. To gain deeper insight into these mechanisms, a 2-D spatiotemporal fast Fourier transform (FFT) analysis on the spatiotemporal displacement fields is performed, as presented in figure 14. Due to the real-valued nature

https://doi.org/10.1017/jfm.2026.11712 Published online by Cambridge University Press

f^*	$\widetilde{U}/U_{ref}$	U_g/U_{ref}	U_w/U_{ref}	f_wL/U_{ref}	λ_w/L
0.51	1.28	1.30	3.56	0.73	4.88
0.57	1.56	1.57	4.86	0.79	6.15
0.64	1.81	1.79	7.46	0.79	9.44

Table 2. The dimensionless average propulsive velocity $\widetilde{U}/U_{ref}$ of the self-propelled plate, the group velocity U_g/U_{ref} of the spatiotemporal spectrum, and the wave speed U_w/U_{ref}, frequency f_wL/U_{ref} and wavelength λ_w/L of the FPTW.

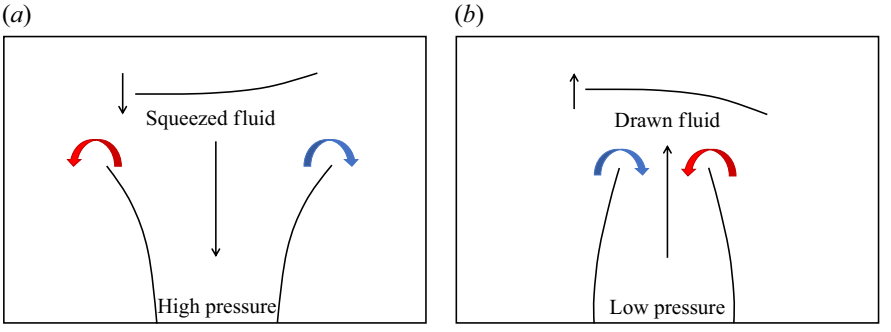


Figure 15. Schematics of the plate–blades interaction process: (*a*) the plate moves downwards; (*b*) the plate moves upwards.

of the displacement signals, the spectra exhibit conjugate symmetry about the origin in the $(k,\ f)$ plane, where k denotes the wavenumber, and f denotes the frequency.

The harmonic components extracted from the FFT align along straight lines, with the slope of these lines (indicated by the red dashed line) defining the group velocity:

$$U_g = -\frac{\mathrm{d}f}{\mathrm{d}k}. \tag{3.19}$$

The negative sign is added because the self-propelled plate moves in the negative x-direction. Physically, the group velocity characterises the propagation velocity of wave packets formed by the superposition of multiple harmonic components, as well as the energy transfer velocity within the vibrating blade array. Notably, the group velocity U_g exhibits good agreement with the average propulsive velocity $\widetilde{U}$ of the self-propelled plate, as summarised in table 2. From the spatiotemporal diagram of blade displacements shown in figure 12, only regime B, where the blade vibrations are directly driven by the flapping motion of the plate, exhibits a wave packet structure that follows the plate's position. The group velocity of the wave packet thus corresponds to the propagation velocity of regime B, and the associated vibration pattern is hereafter termed the flapping-driven mode.

Figure 15 presents two schematics of the interaction between the compliant blades and the nearby flapping plate, thereby offering a physical insight into the flapping-driven mode. As illustrated in figure 15(*a*), when the plate descends towards the blade array, it squeezes fluid into the inter-blade gaps, and induces a local high-pressure region beneath the plate. Due to fluid incompressibility and confinement imposed by adjacent blades, the fluid is forced to escape laterally through the blade tips. This gives rise to tip vortices of opposite signs (anticlockwise at the left tip, clockwise at the right tip), and induces outward blade deformation. Conversely, when the plate ascends and moves away from the blades, as

https://doi.org/10.1017/jfm.2026.11712 Published online by Cambridge University Press

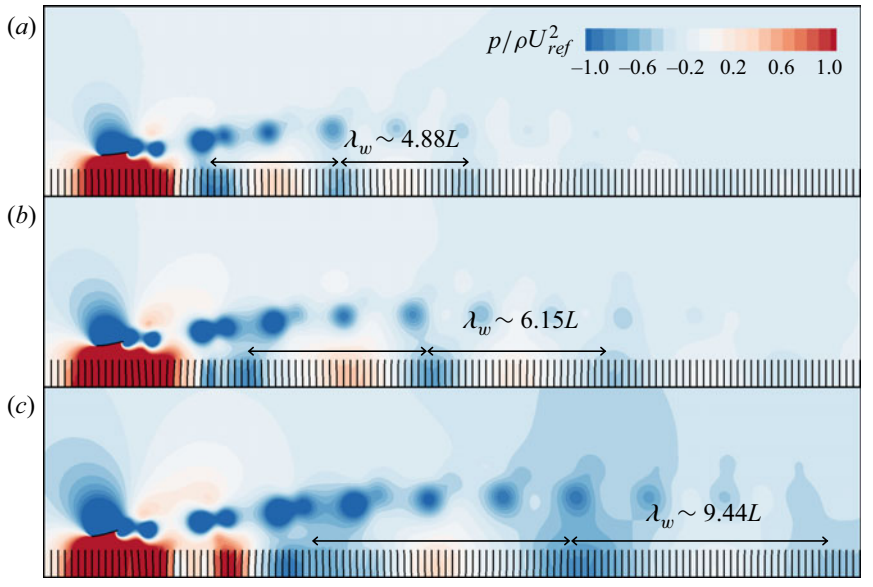


Figure 16. The dimensionless pressure fields at $t/T = 19.00$. The leading edge of the plate is positioned at the average height and is moving downwards. Here, (*a*) $f^* = 0.51$, (*b*) $f^* = 0.57$, (*c*) $f^* = 0.64$. Horizontal arrowed lines mark the wavelength λ_w of the FPTW. Here, $A_L = 0.5$, $H_L = 1.5$, $D_L = 0.25$, $K_p = 3.5$, $K_b = 3.0$. See supplementary movie 2 for the pressure evolution.

illustrated in figure 15(*b*), fluid is drawn from the inter-blade gaps, inducing a local low-pressure region beneath the plate. The replenishing flow enters primarily from the outer sides of the blade tips, generating vortices with reversed rotational directions, and inducing inward blade deformation.

The most energetic spatiotemporal mode, indicated by the red circle in figure 14, exhibits a phase velocity in close agreement with the wave speed U_w of the FPTW, and is thus identified as the FPTW in regime C. Its key parameters, the wave frequency f_w, wavelength $\lambda_w = 1/k_w$, and wave speed $U_w = f_w/k_w$ are listed in table 2. Notably, f_w is almost independent of the flapping frequency f^* of the plate, and approximately equals the natural frequency ($f_n^{inv} L/U_{ref} = 0.73$) of the blades. The λ_w value is significantly larger than the distance travelled by the plate in each flapping period, and it increases dramatically from 4.88 to 9.44 as the flapping frequency f^* of the plate grows from 0.51 to 0.64.

Figure 16 presents the dimensionless pressure fields for different flapping frequencies f^* of the self-propelled plate at $t/T = 19.00$, when the plate's leading edge is positioned at the average height and is moving downwards. A high-pressure region is observed beneath the plate, resulting from the fluid-squeezing effect generated by the downward motion of the plate. Notably, as f^* increases, the spatial extent of the high-pressure region expands. Downstream of the plate, alternating high- and low-pressure regions propagating in the negative x-direction are observed within the blade array (see supplementary movie 2 for the pressure evolution). Furthermore, the spacing between two adjacent low-pressure regions is nearly uniform and exhibits good agreement with the wavelength λ_w of the FPTW, as marked by the arrowed lines in the figures. This observation confirms the strong correlation between the FPTW and the downstream pressure distribution within the blade array. As f^* increases, corresponding to an increase in the propulsive velocity of the plate, the wave speed U_w of the FPTW increases, indicating that U_w is not an intrinsic property

https://doi.org/10.1017/jfm.2026.11712 Published online by Cambridge University Press

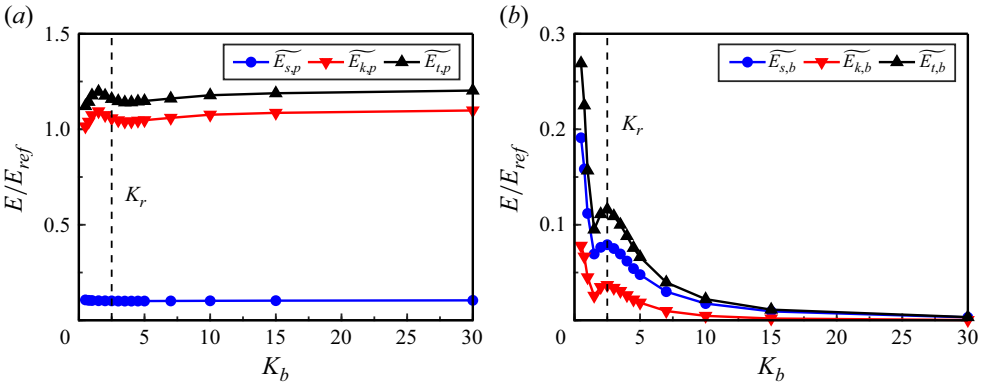


Figure 17. The average strain energy, kinetic energy and mechanical energy of (*a*) the self-propelled plate and (*b*) the compliant blade array as functions of the blade bending stiffness K_b. Here, $f^* = 0.51$, $A_L = 0.5$, $H_L = 1.50$, $D_L = 0.50$, $K_p = 3.5$.

of the blade array, but depends on external excitations. Moreover, the motion of wake vortices has little correlation with the FPTW, indicating that the FPTW originates from the cooperative underdamped vibrations of downstream blades.

3.4. *Resonance between the self-propelled plate and the compliant blade array*

Resonance is a common phenomenon in the forced vibration of elastic structures. To investigate the resonance characteristics in the present system, the strain energy E_s, kinetic energy E_k, and total mechanical energy E_t are computed for both the self-propelled plate and the compliant blade array. For a single elastic beam, E_s is defined similarly to (3.1), and E_k is defined as

$$E_k = \int_0^L 0.5m \left| \frac{\partial \boldsymbol{X}(s,t)}{\partial t} \right|^2 \mathrm{d}s. \tag{3.20}$$

The corresponding energies for the plate are denoted as $E_{s,p}$, $E_{k,p}$ and $E_{t,p} = E_{s,p} + E_{k,p}$. For the blade array, the energies are computed by summing the contributions of all individual blades:

$$E_{s,b} = \sum_{i=1}^{N} E_{s,bi}, \quad E_{k,b} = \sum_{i=1}^{N} E_{k,bi}, \quad E_{t,b} = E_{s,b} + E_{k,b}. \tag{3.21}$$

It is noted that $E_{s,b}$, $E_{k,b}$ and $E_{t,b}$ also vary periodically for $t/T \geq 15$, and the reference energy is defined as $E_{ref} = \rho U_{ref}^2 L^2$.

Figure 17 presents the average strain energy, kinetic energy and total mechanical energy of the plate and the blade array as functions of the blade bending stiffness K_b. For the plate, its average strain energy $\widetilde{E_{s,p}}$ (blue line) is significantly smaller than its average kinetic energy $\widetilde{E_{k,p}}$ (red line), contributing negligibly to the average total mechanical energy $\widetilde{E_{t,p}}$ (black line). As K_b increases, both $\widetilde{E_{k,p}}$ and $\widetilde{E_{t,p}}$ first increase rapidly, then decrease to a local minimum, and finally rise gradually. In contrast, for the blade array, its average strain energy $\widetilde{E_{s,b}}$, average kinetic energy $\widetilde{E_{k,b}}$, and average total mechanical energy $\widetilde{E_{t,b}}$ exhibit the opposing trend: they initially decrease rapidly, then rise to a local maximum, and finally decay gradually to zero as the blades become increasingly rigid. Resonance occurs when $\widetilde{E_{t,b}}$ reaches a local maximum, where the corresponding K_b (marked by the black dashed line) is defined as the resonant bending stiffness K_r. Furthermore, $\widetilde{E_{t,b}}$ is significantly

https://doi.org/10.1017/jfm.2026.11712 Published online by Cambridge University Press

f^*	0.38	0.51	0.64
$f_n^{inv}L/U_{ref}$	0.50	0.66	0.78

Table 3. The dimensionless flapping frequency f^* and the natural frequency $f_n^{inv}L/U_{ref}$ of the compliant blades when resonance occurs.

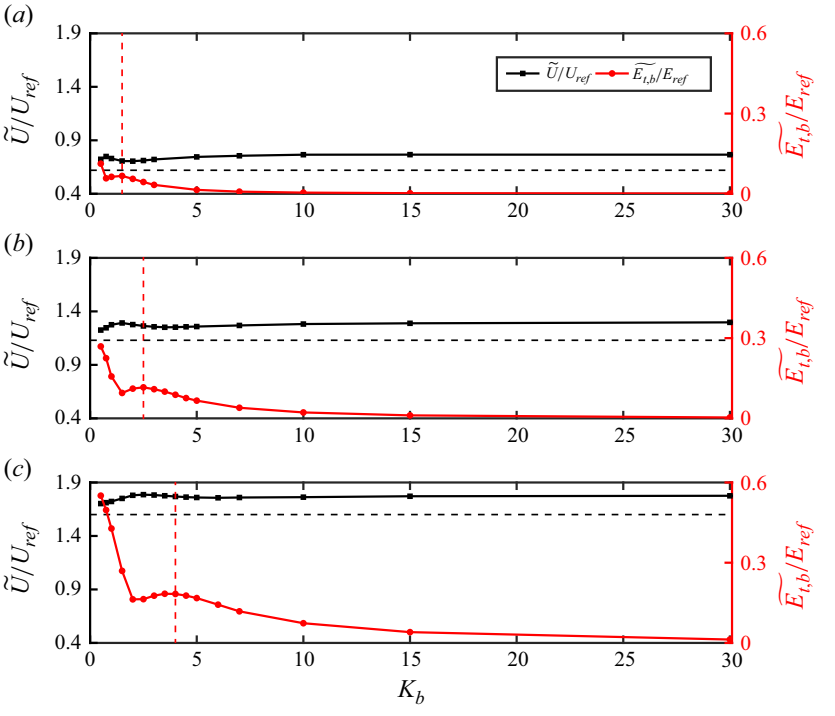


Figure 18. The average propulsive velocity $\widetilde{U}$ of the self-propelled plate, and average mechanical energy $\widetilde{E_{t,b}}$ of the compliant blade array, as functions of the blade bending stiffness K_b, for (*a*) $f^* = 0.38$, (*b*) $f^* = 0.51$, (*c*) $f^* = 0.64$. Here, $A_L = 0.5$, $H_L = 1.5$, $D_L = 0.5$, $K_p = 3.5$. The red dashed lines mark the resonance stiffness K_r. The black dashed lines represent $\widetilde{U}$ of the corresponding cases without blades.

smaller than $\widetilde{E_{t,p}}$, indicating that the energy stored in the blade array accounts for only a small fraction of the total energy in the system.

The resonance phenomenon is also confirmed from the frequency perspective. Table 3 summarises the dimensionless flapping frequency f^* of the self-propelled plate and the natural frequency $f_n^{inv}L/U_{ref}$ of the blades. Here, f_n^{inv} is calculated through (3.17) by setting the dimensionless bending stiffness to K_r. In all cases, f^* is close to but approximately 20 % lower than $f_n^{inv}L/U_{ref}$, a phenomenon also documented in the work of Xiong *et al.* (2024). This is because the resonance frequency of a strongly damped system is lower than its natural frequency without damping, as illustrated in the vibration theory (Rao 2010).

Figure 18 presents the average propulsive velocity $\widetilde{U}$ of the self-propelled plate, and average total mechanical energy $\widetilde{E_{t,b}}$ of the blade array, as functions of the blade bending stiffness K_b. The black dashed lines denote $\widetilde{U}$ for the corresponding cases without blades, and each of them lies below that for the blade-covered wall. Since the magnitudes of $\widetilde{U}$ and

https://doi.org/10.1017/jfm.2026.11712 Published online by Cambridge University Press

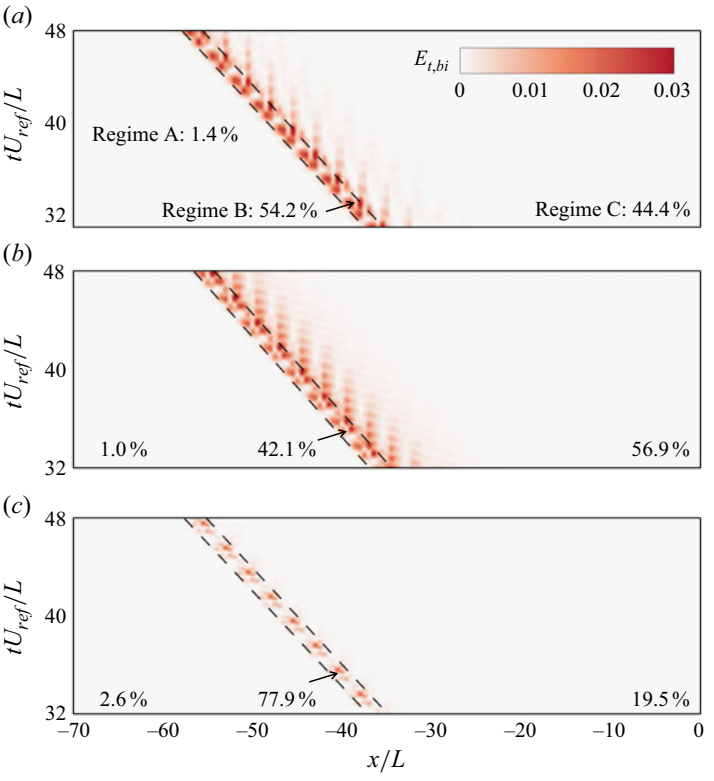


Figure 19. The spatiotemporal distribution of the total mechanical energy $E_{t,bi}$ of the compliant blades, with bending stiffnesses (*a*) $K_b = 1.5$, (*b*) $K_b = 2.5$ (resonance bending stiffness), (*c*) $K_b = 10$. The energy proportions of the three regimes (A, B and C) are marked in the figures. Here, $f^* = 0.51$, $A_L = 0.5$, $D_L = 0.5$, $H_L = 1.5$, $K_p = 3.5$.

$\widetilde{E_{t,b}}$ differ dramatically across the three frequencies, different y-axis ranges are adopted in each subplot to better visualise the respective trends. The variation of $\widetilde{U}$ with K_b exhibits a negative correlation with that of $\widetilde{E_{t,b}}$, i.e. $\widetilde{U}$ first increases rapidly, then decreases to a local minimum, and finally rises gradually with increasing K_b. As the flapping frequency f^* of the plate increases, although both $\widetilde{U}$ and $\widetilde{E_{t,b}}$ increase, the local minimum of $\widetilde{U}$ and local maximum of $\widetilde{E_{t,b}}$ are flattened, and the resonant bending stiffness K_r (marked by red dashed lines) increases. Furthermore, at $f^* = 0.38$, the local minimum of $\widetilde{U}$ nearly coincides with the resonant stiffness K_r; at higher flapping frequencies ($f^* = 0.51$ and 0.64), $\widetilde{U}$ reaches a local minimum at a higher K_b than K_r.

Figure 19 presents the spatiotemporal distribution of the total mechanical energy $E_{t,bi}$ of individual compliant blades at $f^* = 0.51$ for three bending stiffnesses: $K_b = 1.5$, $K_b = K_r = 2.5$ and $K_b = 10$. Being consistent with figure 12, the boundaries of the three regimes A, B and C are marked by black dashed lines. The results indicate that the total mechanical energy of blades in regimes B and C accounts for nearly the entire energy of the blade array. However, their respective proportions vary with K_b. For the blade with $K_b = 1.5$ (softer than the resonant bending stiffness K_r), 54.2 % of the total mechanical energy is distributed in regime B, exceeding that (44.4 %) distributed in regime C. At the resonant stiffness $K_b = K_r = 2.5$, a larger proportion of energy (56.9 %) is distributed in regime C, because the blades undergo more intense excitation and thus store more mechanical energy. For the stiffer blades with $K_b = 10$, the energy is primarily concentrated in regime

https://doi.org/10.1017/jfm.2026.11712 Published online by Cambridge University Press

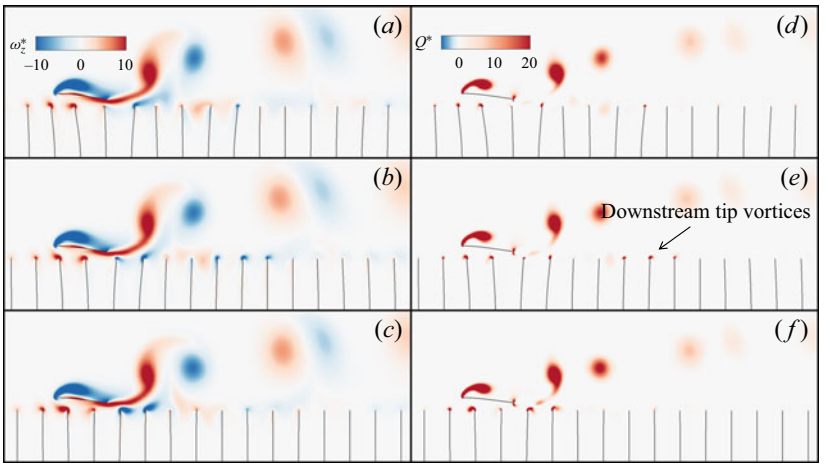


Figure 20. The dimensionless (*a*,*b*,*c*) vorticity field and (*d*,*e*,*f*) Q field ($Q^* = QL^2/U_{ref}^2$) at $t/T = 19.25$ for different blade bending stiffness values: (*a*,*d*) $K_b = 1.5$, (*b*,*e*) $K_b = 2.5$ (resonance bending stiffness), (*c*,*f*) $K_b = 10$. Here, $f^* = 0.51$, $A_L = 0.5$, $H_L = 1.5$, $D_L = 0.5$, $K_p = 3.5$.

B, which accounts for 77.9 % of the total energy. These results demonstrate that resonance facilitates energy storage in downstream regions.

Figure 20 presents distributions of the vorticity and the second invariant of the velocity gradient tensor Q at $t/T = 19.25$ for different blade bending stiffnesses K_b. Here, the positive Q is also used to indicate concentrated vortices, known as the Q-criterion (Hunt, Wray & Moin 1988). Upstream of the leading edge and beneath the plate, the blades are deflected leftwards due to the high-pressure region between the plate and the bottom wall, resulting in the shedding of concentrated positive vortices from the blade tips. As K_b increases, the horizontal displacement of the blade tips decreases progressively; however, the strength of the tip vortices increases. Beneath the trailing-edge vortex and its feeding shear layer, negative vortices are formed at the blade tips. For the resonant case with $K_b = K_r = 2.5$, concentrated tip vortices are observed beyond $2L$ downstream of the plate, confirming that resonance facilitates the vibration of blades in the wake.

4. Conclusion

A numerical investigation is conducted on a self-propelled flexible plate moving above an array of wall-mounted compliant blades, designed to mimic flatfish-like locomotion near a vegetation-covered seabed. This work focuses on two core aspects: the propulsive performance of the plate, and the forced vibration responses of the blade array. The effects of key dimensionless parameters, including the flapping frequency f^* of the plate, blade spacing D_L, vertical distance between the plate and bottom wall H_L, and bending stiffness K_b of the blades, are systematically investigated.

This reveals that the blade array suppresses the deformation of the self-propelled plate while enhancing its propulsive performance, as evidenced by an increase in propulsive velocity and a reduction in cost of transport (*COT*). Such enhancement becomes more pronounced as D_L and H_L decrease, before direct solid–solid contact occurs. Moreover, an increase in flapping frequency of the plate f^* enhances its propulsive velocity at the expense of higher energy consumption. Furthermore, by introducing a correction factor to account for the asymmetric motion of the plate during the upper and lower half-periods,

https://doi.org/10.1017/jfm.2026.11712 Published online by Cambridge University Press

a universal scaling law $Re_c \sim (Re_{f,\delta})^{3/2}$ is identified between the propulsive Reynolds number Re_c and the corrected flapping Reynolds number $Re_{f,\delta}$.

Based on the spatiotemporal diagrams of the blade-tip displacements, three distinct regimes are identified within the blade array. Regime A covers blades upstream of the plate's leading edge, which exhibit negligible vibrations except in the immediate vicinity of the leading edge. Regime B includes blades that are directly excited by the plate over one period, and these blades form a flapping-driven vibration region synchronised with the plate's motion. Regime C consists of downstream blades undergoing underdamped free vibration, where a series of FPTWs arises. These waves are strongly correlated with the pressure distribution within the blade array, and originate from the cooperative underdamped vibration of downstream blades.

Resonance occurs between the flapping plate and the blade array when the flapping frequency of the plate approaches the natural frequency of the blades. At resonance, the blade array absorbs more energy from the system, resulting in a local maximum in its total mechanical energy. Conversely, the propulsive velocity of the plate exhibits a local minimum, which remains higher than that in the corresponding case without blades.

This study yields several implications. First, for underwater swimmers, it is beneficial to leverage the bottom wall to achieve higher propulsive performance, while resonance with surrounding elastic structures should be avoided. Second, the dynamic responses of compliant structures serve as robust indicators of nearby swimmers, offering substantial potential for applications in flow-sensing technologies. Nevertheless, the present investigation is restricted to relatively low Reynolds numbers, and the propulsive performance of near-bottom swimmers at higher Reynolds numbers remains to be systematically explored in future work.

Supplementary movies. Supplementary movies are available at https://doi.org/10.1017/jfm.2026.11712.

Acknowledgements. We thank the University of Science and Technology of China Supercomputing Centre for providing computational resources for this project.

Funding. This work is supported by the National Natural Science Foundation of China (grant nos 12302320, 12388101, 12293000 and 12293002).

Declaration of interests. The authors report no conflict of interest.

Data availability statement. The data that support the findings of this study are available from the corresponding author upon reasonable request.

Appendix A. Dimensionless governing equations and boundary conditions

The dimensionless vertical position of the leading edge of the self-propelled plate is given by

$$y_l^*(t^*) = 0.5A_L \sin(2\pi f^* t^* + \pi) + H_L. \tag{A1}$$

The dimensionless incompressible Navier–Stokes equations and the continuity equation are

$$\frac{\partial \boldsymbol{u}^*}{\partial t^*} + \boldsymbol{u}^* \cdot \nabla^* \boldsymbol{u}^* = -\nabla^* p^* + \frac{1}{100}\nabla^{*2}\boldsymbol{u}^* + \boldsymbol{f}_{IB}^*, \tag{A2}$$

$$\nabla^* \cdot \boldsymbol{u}^* = 0. \tag{A3}$$

https://doi.org/10.1017/jfm.2026.11712 Published online by Cambridge University Press

The dimensionless time, velocity, pressure and volume force are defined as

$$t^* = \frac{tU_{ref}}{L}, \quad \boldsymbol{u}^* = \frac{\boldsymbol{u}}{U_{ref}}, \quad p^* = \frac{p}{\rho U_{ref}^2}, \quad \boldsymbol{f}_{IB}^* = \frac{L\boldsymbol{f}_{IB}}{\rho U_{ref}^2}. \tag{A4}$$

The dimensionless governing equation for the beam is given by

$$\rho^* \frac{\partial^2 \boldsymbol{X}^*}{\partial t^{*2}} - S\frac{\partial}{\partial s^*}\left[\left(1 - \left|\frac{\partial \boldsymbol{X}^*}{\partial s^*}\right|^{-1}\right)\frac{\partial \boldsymbol{X}^*}{\partial s^*}\right] + K\frac{\partial^4 \boldsymbol{X}^*}{\partial s^{*4}} = \boldsymbol{F}_{IB}^*. \tag{A5}$$

The boundary condition at the leading edge of the self-propelled plate is given by

$$\left.\frac{\partial X_p^*}{\partial s^*}\right|_{s^*=0} = 1, \quad \left.\frac{\partial Y_p^*}{\partial s^*}\right|_{s^*=0} = 0, \quad Y_p^*(0, t^*) = y_l^*(t^*). \tag{A6}$$

Meanwhile, the boundary conditions at the root of the ith blade are given by

$$\left.\frac{\partial X_{bi}^*}{\partial s^*}\right|_{s^*=0} = 0, \quad \left.\frac{\partial Y_{bi}^*}{\partial s^*}\right|_{s^*=0} = 1, \quad X_{bi}^*(0, t^*) = -i\,D_L, \quad Y_{bi}^*(0, t^*) = 0. \tag{A7}$$

At the free ends of the plate and blades, the following boundary conditions are applied:

$$\left[S\left(1 - \left|\frac{\partial \boldsymbol{X}^*}{\partial s^*}\right|^{-1}\right)\frac{\partial \boldsymbol{X}^*}{\partial s^*} - K\frac{\partial^3 \boldsymbol{X}^*}{\partial s^{*3}}\right]_{s^*=1} = \boldsymbol{0}, \quad \left.\frac{\partial^2 \boldsymbol{X}^*}{\partial s^{*2}}\right|_{s^*=1} = \boldsymbol{0}. \tag{A8}$$

The dimensionless position vector and external force are defined as

$$\boldsymbol{X}^* = \frac{\boldsymbol{X}}{L}, \quad s^* = \frac{s}{L}, \quad \boldsymbol{F}_{IB}^* = \frac{\boldsymbol{F}_{IB}}{\rho U_{ref}^2}. \tag{A9}$$

References

Ackerman, J.D. & Okubo, A. 1993 Reduced mixing in a marine macrophyte canopy. *Funct. Ecol.* **7** (3), 305–309.

Alben, S. 2008 Optimal flexibility of a flapping appendage in an inviscid fluid. *J. Fluid Mech.* **614**, 355–380.

Alben, S., Witt, C., Baker, T.V., Anderson, E. & Lauder, G.V. 2012 Dynamics of freely swimming flexible foils. *Phys. Fluids* **24** (5), 051901.

Ayancik, F., Zhong, Q., Quinn, D.B., Brandes, A., Bart-Smith, H. & Moored, K.W. 2019 Scaling laws for the propulsive performance of three-dimensional pitching propulsors. *J. Fluid Mech.* **871**, 1117–1138.

Brunetto, P., Fortuna, L., Graziani, S. & Strazzeri, S. 2008 A model of ionic polymer–metal composite actuators in underwater operations. *Smart Mater. Struct.* **17** (2), 025029.

Chen, S. & Doolen, G.D. 1998 Lattice Boltzmann method for fluid flows. *Annu. Rev. Fluid Mech.* **30** (1), 329–364.

Connell, B.S.H. & Yue, D.K.P. 2007 Flapping dynamics of a flag in a uniform stream. *J. Fluid Mech.* **581**, 33–67.

Dai, L., He, G. & Zhang, X. 2016 Self-propelled swimming of a flexible plunging foil near a solid wall. *Bioinspir. Biomim.* **11** (4), 046005.

Dibble, E.D., Killgore, K.J. & Harrel, S.L. 1996 Assessment of fish–plant interactions. In *Multidimensional Approaches to Reservoir Fisheries Management* (ed. L.E. Miranda & D.R. DeVries), vol. 16, pp. 357–372. Amer Fisheries Soc.

Doyle, J.F. 2001 *Nonlinear Analysis of Thin-Walled Structures: Statics, Dynamics, and Stability*. Springer Science & Business Media.

Floryan, D., Van Buren, T., Rowley, C.W. & Smits, A.J. 2017 Scaling the propulsive performance of heaving and pitching foils. *J. Fluid Mech.* **822**, 386–397.

Foggi Rota, G., Monti, A., Olivieri, S. & Rosti, M.E. 2024 Dynamics and fluid–structure interaction in turbulent flows within and above flexible canopies. *J. Fluid Mech.* **989**, A11.

Fox, C.H., Gibb, A.C., Summers, A.P. & Bemis, W.E. 2018 Benthic walking, bounding, and maneuvering in flatfishes (pleuronectiformes: pleuronectidae): new vertebrate gaits. *Zoology* **130**, 19–29.

https://doi.org/10.1017/jfm.2026.11712 Published online by Cambridge University Press

FU, J., HE, G., HUANG, L., DEY, S. & FANG, H. 2023 Swaying motions of submerged flexible vegetation. *J. Fluid Mech.* **971**, A14.
GAO, T. & LU, X.-Y. 2008 Insect normal hovering flight in ground effect. *Phys. Fluids* **20** (8), 087101.
GAZZOLA, M., ARGENTINA, M. & MAHADEVAN, L. 2014 Scaling macroscopic aquatic locomotion. *Nat. Phys.* **10** (10), 758–761.
GHISALBERTI, M. & NEPF, H.M. 2002 Mixing layers and coherent structures in vegetated aquatic flows. *J. Geophys. Res.: Oceans* **107**, C2.
GIBSON, R.N., STONER, A.W. & RYER, C.H. 2014 The behaviour of flatfishes. In *Flatfishes: Biology and Exploitation* (ed. R.N. Gibson, R.D.M. Nash, A.J. Geffen & H.W. van der Veer), chap. 12, pp. 314–345. John Wiley & Sons, Ltd.
GOLDSTEIN, D., HANDLER, R. & SIROVICH, L. 1993 Modeling a no-slip flow boundary with an external force field. *J. Comput. Phys.* **105** (2), 354–366.
HAN, T., ZHONG, Q., MIVEHCHI, A., QUINN, D.B. & MOORED, K.W. 2024 Revealing the mechanism and scaling laws behind equilibrium altitudes of near-ground pitching hydrofoils. *J. Fluid Mech.* **978**, A5.
HE, P. 2003 Swimming behaviour of winter flounder (*Pleuronectes americanus*) on natural fishing grounds as observed by an underwater video camera. *Fish. Res.* **60** (2), 507–514.
HE, S., LIU, H. & SHEN, L. 2022 Simulation-based study of turbulent aquatic canopy flows with flexible stems. *J. Fluid Mech.* **947**, A33.
HUA, R.-N., ZHU, L. & LU, X.-Y. 2013 Locomotion of a flapping flexible plate. *Phys. Fluids* **25** (12), 121901.
HUANG, W.-X., SHIN, S.J. & SUNG, H.J. 2007 Simulation of flexible filaments in a uniform flow by the immersed boundary method. *J. Comput. Phys.* **226** (2), 2206–2228.
HUNT, J.C.R., WRAY, A.A. & MOIN, P. 1988 Eddies, streams, and convergence zones in turbulent flows. In *Studying Turbulence Using Numerical Simulation Databases, 2. Proceedings of the 1988 Summer Program*, pp. 193–208. Center for Turbulence Research, Stanford University.
JEONG, Y.D., LEE, J.H. & PARK, S.G. 2021 Flow-mediated interactions between two self-propelled flexible fins near sidewalls. *J. Fluid Mech.* **913**, A39.
LIN, X., WU, J. & ZHANG, T. 2021 Self-directed propulsion of an unconstrained flapping swimmer at low Reynolds number: hydrodynamic behaviour and scaling laws. *J. Fluid Mech.* **907**, R3.
LIU, K., DING, M., PAN, B., YU, P., LU, D., CHEN, S., ZHANG, S. & WANG, G. 2024 A maneuverable underwater vehicle for near-seabed observation. *Nat. Commun.* **15** (1), 10284.
LIU, K., LIU, X. & HUANG, H. 2022 Scaling the self-propulsive performance of pitching and heaving flexible plates. *J. Fluid Mech.* **936**, A9.
LUO, X.-G., GAO, A.-K. & LU, X.-Y. 2023 Enhanced performance of a self-propelled flexible plate by a uniform shear flow and mechanism insight. *Phys. Fluids* **35** (2), 021903.
MITTAL, R. & IACCARINO, G. 2005 Immersed boundary methods. *Annu. Rev. Fluid Mech.* **37** (1), 239–261.
MOYLE, P.B. & CECH, J.J. JR 2004 *Fishes: An Introduction to Ichthyology*, 5th edn. Pearson Prentice Hall.
NI, J., ZHANG, Z., JI, C., XU, D. & ZHANG, X. 2025 Evolution of large-scale vortices and its influence on flow and flexible vegetation dynamics of a finite-length canopy in a 2-D laminar flow. *J. Fluid Mech.* **1017**, A2.
NOWROOZI, B.N., STROTHER, J.A., HORTON, J.M., SUMMERS, A.P. & BRAINERD, E.L. 2009 Whole-body lift and ground effect during pectoral fin locomotion in the northern spearnose poacher (*Agonopsis vulsa*). *Zoology* **112** (5), 393–402.
O'CONNOR, J. & REVELL, A. 2019 Dynamic interactions of multiple wall-mounted flexible flaps. *J. Fluid Mech.* **870**, 189–216.
O'LEARY, J.K., GOODMAN, M.C., WALTER, R.K., WILLITS, K., PONDELLA, D.J. & STEPHENS, J. 2021 Effects of estuary-wide seagrass loss on fish populations. *Estuar. Coast.* **44** (8), 2250–2264.
OSSE, J.W.M. & VAN DEN BOOGAART, J.G.M. 1997 Size of flatfish larvae at transformation, functional demands and historical constraints. *J. Sea Res.* **37** (3–4), 229–239.
PARK, S.G., KIM, B. & SUNG, H.J. 2017 Hydrodynamics of a self-propelled flexible fin near the ground. *Phys. Fluids* **29** (5), 051902.
PENG, Z.-R., HUANG, H. & LU, X.-Y. 2018 Hydrodynamic schooling of multiple self-propelled flapping plates. *J. Fluid Mech.* **853**, 587–600.
PENG, Z.-R., SUN, Y., YANG, D., XIONG, Y., WANG, L. & WANG, L. 2022 Scaling laws for drag-to-thrust transition and propulsive performance in pitching flexible plates. *J. Fluid Mech.* **941**, R2.
PESKIN, C.S. 2002 The immersed boundary method. *Acta Numerica* **11**, 479–517.
QUINN, D.B., MOORED, K.W., DEWEY, P.A. & SMITS, A.J. 2014 Unsteady propulsion near a solid boundary. *J. Fluid Mech.* **742**, 152–170.
RAO, S.S. 2010 *Mechanical Vibrations*, 5th edn. Pearson.
SMITS, A.J. 2019 Undulatory and oscillatory swimming. *J. Fluid Mech.* **874**, P1.

https://doi.org/10.1017/jfm.2026.11712 Published online by Cambridge University Press

STONER, A.W. & TITGEN, R.H. 2003 Biological structures and bottom type influence habitat choices made by Alaska flatfishes. *J. Expl Mar. Biol. Ecol.* **292** (1), 43–59.

TANG, C., HUANG, H., GAO, P. & LU, X.-Y. 2016 Self-propulsion of a flapping flexible plate near the ground. *Phys. Rev. E* **94**, 033113.

TIAN, F.-B., LUO, H., ZHU, L., LIAO, J.C. & LU, X.-Y. 2011 An efficient immersed boundary–lattice Boltzmann method for the hydrodynamic interaction of elastic filaments. *J. Comput. Phys.* **230** (19), 7266–7283.

TSCHISGALE, S., LÖHRER, B., MELLER, R. & FRÖHLICH, J. 2021 Large eddy simulation of the fluid–structure interaction in an abstracted aquatic canopy consisting of flexible blades. *J. Fluid Mech.* **916**, A43.

VAN EYSDEN, C.A. & SADER, J.E. 2006 Resonant frequencies of a rectangular cantilever beam immersed in a fluid. *J. Appl. Phys.* **100** (11), 114916.

VAN KATWIJK, M.M., BOS, A.R., HERMUS, D.C.R. & SUYKERBUYK, W. 2010 Sediment modification by seagrass beds: muddification and sandification induced by plant cover and environmental conditions. *Estuar. Coast. Shelf Sci.* **89** (2), 175–181.

WANG, J., HE, G., DEY, S. & FANG, H. 2022*a* Fluid–structure interaction in a flexible vegetation canopy in an open channel. *J. Fluid Mech.* **951**, A41.

WANG, J., HE, G., DEY, S. & FANG, H. 2022*b* Influence of submerged flexible vegetation on turbulence in an open-channel flow. *J. Fluid Mech.* **947**, A31.

WEBB, P.W. 1993 The effect of solid and porous channel walls on steady swimming of steelhead trout *Oncorhynchus mykiss*. *J. Expl Biol.* **178** (1), 97–108.

WEBB, P.W. 2002 Kinematics of plaice, *Pleuronectes platessa*, and cod, *Gadus morhua*, swimming near the bottom. *J. Expl Biol.* **205** (14), 2125–2134.

XIONG, Y.-H., GAO, A.-K., LU, X.-Y. & CHEN, S. 2024 Numerical study of the oscillatory boundary layer over wall-mounted flexible filaments. *Phys. Rev. Fluids* **9**, 124101.

YANG, G., LI, W.-J., DU, H.-B., WAN, Y., JIA, R., YANG, S.-F. & ZHANG, P. 2024 The influence of wall effects on self-propelled performance of brown trout swimming. *Phys. Fluids* **36** (4), 041907.

ZHANG, C., GAO, A.-K. & ZHU, X. 2026 Flapping dynamics of a compliant membrane in a uniform incoming flow. *J. Fluid Mech.* **1027**, A31.

ZHANG, C., HUANG, H. & LU, X.-Y. 2017 Free locomotion of a flexible plate near the ground. *Phys. Fluids* **29** (4), 041903.

ZHANG, C., HUANG, H. & LU, X.-Y. 2020*a* Effect of trailing-edge shape on the self-propulsive performance of heaving flexible plates. *J. Fluid Mech.* **887**, A7.

ZHANG, X., HE, G. & ZHANG, X. 2020*b* Fluid–structure interactions of single and dual wall-mounted 2D flexible filaments in a laminar boundary layer. *J. Fluids Struct.* **92**, 102787.

ZHONG, Q., HAN, T., MOORED, K.W. & QUINN, D.B. 2021 Aspect ratio affects the equilibrium altitude of near-ground swimmers. *J. Fluid Mech.* **917**, A36.

ZHU, X., HE, G. & ZHANG, X. 2014 Flow-mediated interactions between two self-propelled flapping filaments in tandem configuration. *Phys. Rev. Lett.* **113**, 238105.

https://doi.org/10.1017/jfm.2026.11712 Published online by Cambridge University Press